ELSEVIER

Contents lists available at ScienceDirect

Acta Materialia

journal homepage: www.elsevier.com/locate/actamat



Full length article

Complexity and evolution of a three-phase eutectic during coarsening uncovered by 4D nano-imaging

George R. Lindemann ^a, Paul Chao ^a, Viktor Nikitin ^b, Vincent De Andrade ^b, Marc De Graef ^c, Ashwin J. Shahani ^{a,d,*}

- ^a Department of Materials Science and Engineering, University of Michigan, Ann Arbor, MI 48109, USA
- b Advanced Photon Source, Argonne National Laboratory, Lemont, IL 60439, USA
- ^c Department of Materials Science and Engineering, Carnegie Mellon University, Pittsburgh, PA 15213, USA
- ^d Department of Chemical Engineering, University of Michigan, Ann Arbor, MI 48109, USA

ARTICLE INFO

Keywords: Coarsening Ostwald ripening Solid-state transformation Multi-phase eutectics Real-time imaging X-ray nano-tomography Crystallography

ABSTRACT

We investigate the coarsening dynamics of the three-phase eutectic $Al-Ag_2Al-Al_2Cu$ at 723 K *via in situ* transmission X-ray nano-tomography. Unlike previous investigations that compared observations between different samples annealed for different times, our three-dimensional measurement shows at nanoscale resolution the microstructural changes occurring in the same field-of-view, enabling new insight on the capillary-driven evolution of a ladder-like pattern. With the aid of a new reconstruction algorithm and machine learning segmentation, we trace the interfaces of the eutectic and observe significant structural changes within 4 hr. of aging. Even though the average length-scales of the eutectic solids follow a temporal power law, the microstructure is not self-similar. Instead, it evolves (in part) through the coalescence of neighboring Ag_2Al solids at the expense of the intervening Al_2Cu . By combining our X-ray data with electron diffraction to identify the common planes at the interphase boundaries, we show that coalescence leads to a decrease in lattice misfit, and hence, interfacial energy. At longer times, the interphase boundaries with low misfit compete for surface area, resulting in a 'locking' of the interfacial shape.

1. Introduction

Naturally occurring, multi-phase eutectic alloys have composite-like properties [1,2], beneficial for many technological applications. This has sparked renewed scientific interest in understanding how they nucleate and grow [3–6]. However, we currently have limited knowledge on how the increased number of solid phases in these multi-phase alloys influences the coarsening process *after* eutectic solidification. Many of these materials operate at elevated temperatures wherein their microstructures and properties change over time, often to the detriment of reliability [7–13]. Likewise, in additive manufacturing, the transient thermal gradients in the heat-affected zone may lead to a microstructural evolution *via* coarsening that may influence the load transfer between phases [14–17]. Therefore, it is crucial to have a thorough understanding of the coarsening process in these materials to predict how they might evolve during their life-cycle.

In the absence of a chemical driving force for precipitation, solidstate microstructural evolution is driven purely by a reduction of interfacial free energy. Depending on the material system and characteristic coarsening length, this process can cause changes in both morphology and bicrystallography, resulting in different features at different stages. When annealed below the eutectic temperature, eutectic microstructures coarsen continuously in the solid-state *via* Ostwald ripening, Rayleigh instabilities, and fault migration [18]. The eutectic may also undergo *discontinuous* coarsening, in which the original eutectic cells or grains are replaced by new ones with larger interphase spacing [19].

Elementary mechanisms of coarsening in two-phase systems. The mechanism of continuous coarsening depends on the interfacial structure. If the Wulff shape is isotropic, the interfaces are curved and the eutectic coarsens via curvature reduction, as depicted in Fig. 1(a). In contrast, some eutectic alloys have faceted rods or plates due to their anisotropic solid–solid interfacial free energy [20,21]. Examples of such alloys include Bi-In-Sn [22,23], Zn-Mg-Al [24], and Al-Ag-Cu [25,26]. Facets on rods may form to reduce their interfacial surface energy by aligning with a low energy crystallographic plane during annealing [9,27], see Fig. 1(b). In such a scenario, we may also expect that the faceted rods are resistant to Rayleigh instabilities since any perturbation would require the creation of surfaces with higher interfacial energies. As

^{*} Corresponding author at: Department of Materials Science and Engineering, University of Michigan, Ann Arbor, MI 48109, USA. E-mail address: shahani@umich.edu (A.J. Shahani).

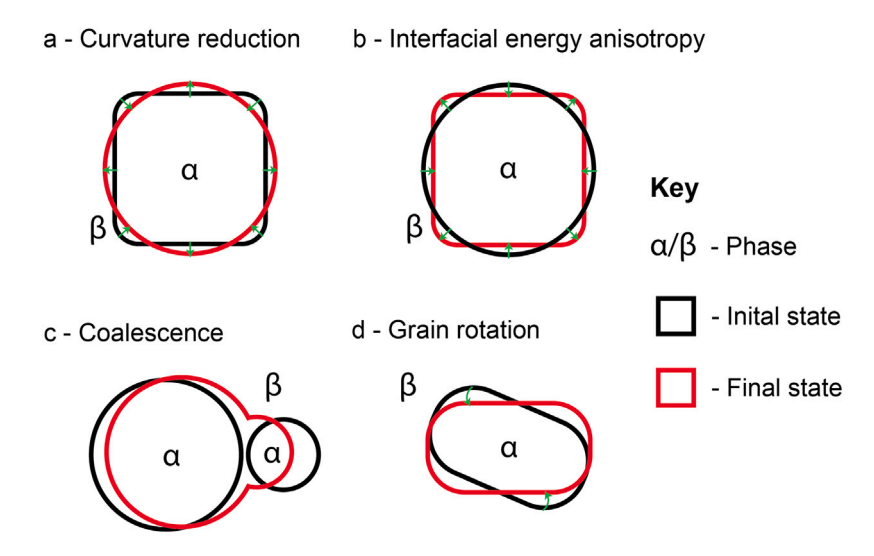


Fig. 1. Four elementary mechanisms of solid-state coarsening, as depicted in the schematics. a Curvature reduction dissipates surface energy by removing regions of high curvature (see arrows). b Interfacial energy anisotropy drives a particle or grain to align along low energy crystal orientations (oftentimes producing facets). c Coalescence enables two particles/grains to fuse into a single entity, thereby removing the high misfit boundaries in the channel between them. d Grain rotation reconfigures grains to a lower energy state with their surrounding neighbors by aligning to lower misfit planes. The two phases are α and β throughout; the black color gives the initial state, while the red shows the final state

such, faceted phases tend to coarsen through 2D Ostwald ripening or through fault migration [27]. It is also possible for faceted eutectic rods to reduce their interfacial energy by coalescing along relatively high energy planes (Fig. 1(c)) [28,29] or rotating to align with a low energy orientation (Fig. 1(d)) [12,30].

Role of multiple solid phases on the coarsening dynamics. Beyond the interfacial structure, we must also account for the effect of other dispersed solid phases in a multi-phase system. For example, consider a material consisting of β and γ phase 'particles' embedded in an α phase matrix. The growth of each particle depends on the solute sources and sinks. Holmes [31,32] describes three possible scenarios for particle interaction based on their so-called cross coupling coefficients, $\Gamma_{n,p}$, defined as

$$\Gamma_{n,p} = \frac{D_{j} \Delta c_{i}^{m,n} \Delta c_{i}^{m,p} + D_{i} \Delta c_{j}^{m,n} \Delta c_{j}^{m,p}}{D_{j} (\Delta c_{i}^{m,n})^{2} + D_{i} (\Delta c_{j}^{m,n})^{2}}$$
(1)

where D_i and $\Delta c_i^{m,n}$ are the diffusivities and equilibrium concentration differences of component i, respectively, in which the subscript indicates the solute, m is the matrix phase, and n and p are the dispersed solid precipitates. If $\Gamma_{n,p} \to 0$, the particles experience a weak coupling. This means that the β and γ produce small or non-existent solute depletion zones, leading to a spatial correlation of β and γ particles. When $\Gamma_{n,p} \geq 1$, the particles display a strong positive coupling. In this case, β particles have greater interaction with neighboring γ particles than with other β particles. This leads to a highly segregated microstructure, wherein large regions of β are broken up by veins of γ . Finally, strong negative coupling occurs when $\Gamma_{n,p} \ll 0$. In this scenario, β and γ particles act as solute sources, resulting in growing β particles neighboring growing γ particles, and large regions devoid of precipitates appear within the material as particles of both phases are consumed through bulk diffusion.

Allen et al. conducted a study on the time-evolution of a Sn-Ag–Cu eutectic alloy that consisted of three phases: Sn (matrix), Cu₆Sn₅ (rods), and Ag₃Sn (plates) [7,8]. The overall eutectic coarsened according to an $r^3 \propto t$ relationship, which they attributed to bulk Cu diffusion. That said, the two intermetallic phases, Cu₆Sn₅ and Ag₃Sn, coarsened at different rates and independently from one another (*i.e.*, $\Gamma_{n,p} \rightarrow 0$), such that the rate-controlling mechanism is the same in ternary and binary systems: Ostwald ripening for Cu₆Sn₅ and spheroidization for Ag₃Sn, mediated by interface diffusion of Ag along the Ag₃Sn/Sn interphase boundary. This study provided support for the above model, which

predicted weak coupling between Cu_6Sn_5 and Ag_3Sn phases due to the low mutual solubilities.

The above results suggest that, in order to predict how the microstructure in multi-phase and multi-component eutectic alloys will coarsen, we must follow the evolution of three or more solid-solid interfaces and map an even more complex diffusion field in space and time. Previous studies on multi-component systems have mostly focused on the coarsening of dispersed particles [7,8,31-34], rather than the evolution of eutectic alloys (particularly in symmetrical phase diagrams), with a few exceptions [5,35]. Importantly, one cannot necessarily assume infinite dilution for eutectics, since the solid phases are separated by a characteristic spacing that is on the order of a few micrometers. Due to the increasing demand for multi-phase eutectics [22, 36,37], and recent improvements in real-time imaging capabilities [38– 41], the time is ripe to understand the dynamics of coarsening in such morphologically and topologically complex systems. For this purpose, the Al-Ag₂Al-Al₂Cu eutectic is ideal: it has well-established thermophysical properties [25,26,42-49], and a relatively low eutectic temperature (T_e) of 773.15 K; in addition, there has been preliminary work on post-solidification microstructural evolution [35,50]. Lastly, the Al-Ag₂Al-Al₂Cu eutectic forms multiple unique eutectic patterns [43, 45,51] depending on the alloy composition and growth velocity in directional solidification. This provides different initial conditions that may lead to different end-products upon coarsening.

Despite the extensive research on the Al-Ag₂Al-Al₂Cu three-phase eutectic, many questions remain unanswered about its solid-state evolution. Specifically, what mechanism(s) drive solid-state coarsening in the system, and do multiple rate-limiting mechanisms coexist, as seen in the aforementioned Sn-Ag–Cu eutectic alloy [7,8]? Additionally, how does the interfacial anisotropy influence the solid-state evolution? For example, do established low energy interphase boundaries compete with curvature reduction to slow or stop coarsening?

With the aim of answering these questions, we used synchrotron-based X-ray nano-tomography to obtain a three-dimensional (3D) view of the microstructural evolution and EBSD to track crystallographic evolution in $Al-Ag_2Al-Al_2Cu$. The former imaging technique allows all three solid phases to be distinguished readily [26,52,53], owing to the differences in attenuation contrast, and at high resolution (45 nm/pixel). Conventional micro-tomography is not suitable since the lamellar spacing is on the order of a few micrometers in directional solidification (DS), *i.e.*, approaching the pixel size (0.69 μ m) [54].

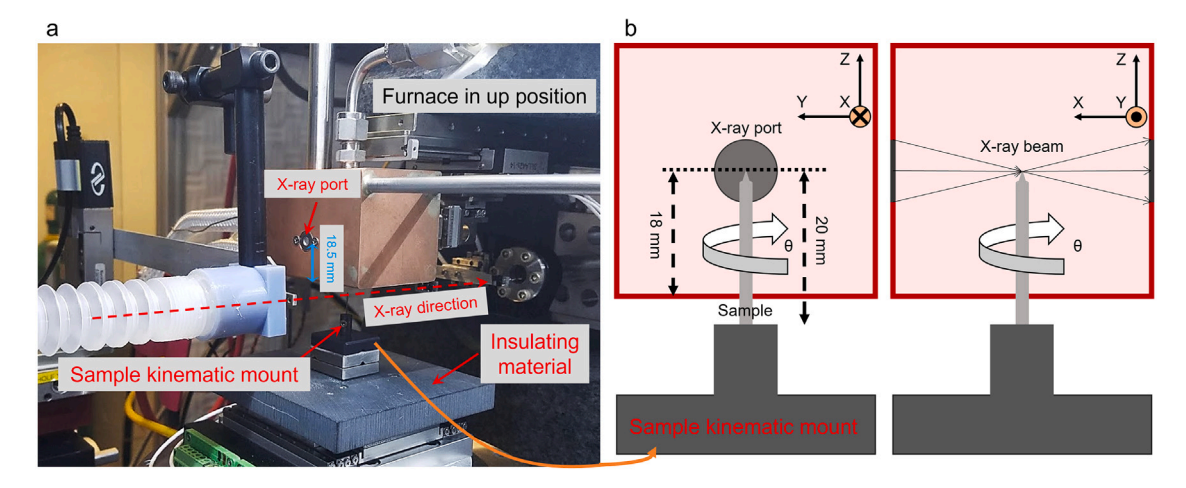


Fig. 2. Experimental setup for synchrotron TXM, at elevated temperatures at APS beam-line 32-ID. At left is a photograph of furnace used for in situ viewing. Red arrows indicate the X-ray port and direction of the X-ray beam. The sample is placed inside this furnace and rotated to capture images from different views, see schematics at right.

Instead, our multimodel nano-imaging study focuses on characterizing the morphological and crystallographic evolution in a pseudo-ladder three-phase eutectic pattern [44,45], and the correlation of the two. Our efforts are made possible thanks to new hardware developments (a resistive heater at the synchrotron beam-line, enabling *in situ* experimentation) and new opportunities for multimodal characterization (the integration of X-ray absorption and electron diffraction data [54]). These advances enable us to obtained detailed insight on the coarsening mechanism, interfacial anisotropy, and time-dependent bicrystal lattice mismatch.

2. Methods

2.1. In situ synchrotron X-ray nano-tomography

An alloy of composition Al-42.2 wt%Ag-17.6 wt%Cu (corresponding to the three-phase eutectic point [47]) was produced using high purity elements (99.999% Al, 99.999% Ag, and 99.999% Cu), vacuum arc remelted at the Materials Preparation Center at Ames Laboratory (Ames, IA, USA). A cylindrical rod 1 mm in diameter and 10 mm in length was cut from the ingot using electron discharge machining (EDM). The rod was then placed into an alumina crucible and solidified within a vertical three-zone Bridgman directional furnace (MTI Corporation EQ-SKJ-BG). Since the sample diameter was small, radial convection is negligible in DS [55]. In practice, the sample was directionally solidified *via* the 'gradient freeze' method by imposing a cooling rate, $\frac{dT}{dt}$, of ~0.9 K/min on each zone under a fixed thermal gradient, G, of ~1.5 K/mm anti-parallel to gravity. Under these conditions, the sample was expected to grow at a velocity, V, of ~10 μ m/s. Following DS, we turned off the furnaces and removed the sample, allowing it to cool in air to room temperature.

Following DS, we hand polished and radially sectioned the sample, hereafter referred to as 'as-cast', approximately halfway along its length. With scanning electron microscopy (SEM), we identified a pseudo-ladder three-phase eutectic morphology [44,45]. Using Xe plasma focused ion beam (FIB) milling, we milled a ~45 μm diameter pillar of this material for *in situ* synchrotron X-ray nano-tomography with the Transmission X-ray Microscope (TXM) instrument. The experiments were performed at beamline 32-ID at the Advanced Photon Source of Argonne National Laboratory (Lemont, IL, USA) [56,57]. We secured the sample onto an alumina rod with boron nitride spray and placed it on the kinematic mount (see Fig. 2). Subsequently, we heated our sample to a homologous temperature of $0.9T_e$ (with respect to the three-phase eutectic temperature of 773.15 K) and annealed it isothermally for 4 hr. To capture the transient eutectic microstructure during coarsening, we took six intermittent TXM scans of the sample

at 0.5, 0.75, 1, 2, 3, and 4 hr. time-steps at temperature, i.e., without quenching the sample, in addition to an initial or 0 hr. scan at room temperature. For the TXM measurements we used a 50 nm outerzone width Fresnel Zone plate (FZP) coupled with a mono-capillary condenser. The detector had 2448×2048 pixels, with 45 nm pixel size after magnification. 1004 tomographic projections were acquired while rotating the samples over 180 degrees. X-ray exposure time per each projection was 0.5 s, resulting in 8.4 min. time per scan. We attempted a continuous or uninterrupted scan between the 0 and 30 min. scans. To prevent blurring artifacts in the reconstruction domain associated with fast-moving features [54], we reduced the exposure time to 0.1 s. Unfortunately, however, this resulted in a poor spatial resolution such that we were not able to distinguish the solid-solid interphase boundaries. For this reason, we do not analyze this particular dataset further. Throughout, we used a monochromatic beam of 8.4 keV to achieve reasonable contrast between the three phases.

That said, the high-temperature environment caused significant vibrations that were detrimental to the image resolution. This led to thermal radiation-induced deformations in the X-ray projection images. As a result, when we employed a standard algorithm to reconstruct our tomographic data, the data irregularities propagated into the reconstructed domain, making it difficult to separate phases and trace interfaces. To address this challenge, we used a new technique for compensating sample deformation artifacts and reducing the noise level [58]. In the following section, we will provide a brief description of this technique.

2.2. Optimized tomographic reconstruction

With a conventional method such as Gridrec implemented in the Tomopy package [59], a 3D object x can be reconstructed from its projection data d, according to

$$x = \mathcal{R}^* \mathcal{W} d, \tag{2}$$

where \mathcal{R}^* is the adjoint Radon transform operator and \mathcal{W} is a filter, see [60] for details. The method has the property of amplifying noise in images due to the filter structure. Therefore, reconstruction in many cases is performed by solving the following optimization problem,

$$\min_{\mathbf{x}} \|\mathcal{R}\mathbf{x} - d\|^2 \tag{3}$$

using iterative schemes and without the filtering operation. Commonly used iterative schemes for solving Eq. (3) include the conjugate gradients method and simultaneous algebraic reconstruction technique [61]. In order to compensate for sample nano-drifts and decrease the noise level, we followed the method in Ref. [58] and modified Eq. (3)

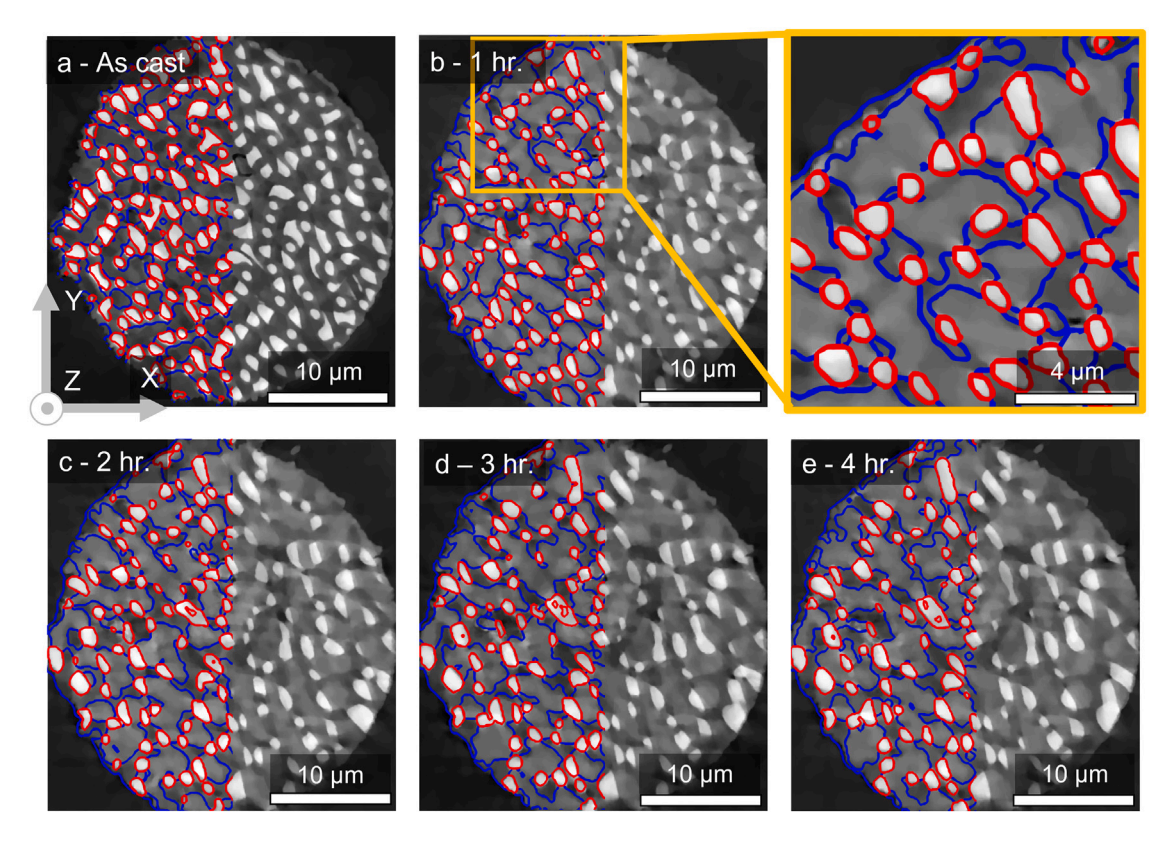


Fig. 3. Reconstruction slices provide snapshots of the microstructural evolution, at a 0, b 1, c 2, d 3, and e 4 hr. of annealing. A magnified view of pseudo-ladder pattern in b is shown in yellow boxed region. This particular, representative slice (see coordinate system in a) is located $\sim 6.5~\mu m$ below the top of the micropillar sample. In a, the dark gray color represents Al, the light gray Al_2Cu , and white Al_2Cu are outlined in red and blue, respectively, on the left-hand side.

by adding the total variation (TV) regularization term $\|\nabla x\|_1$ and local deformation estimation operator \mathcal{D}_s that map functions to new coordinates according to local shifts s,

$$\min_{x,s} \|\mathcal{D}_s \mathcal{R} x - d\|_2 + \lambda \|\nabla x\|_1, \tag{4}$$

where the parameter λ corresponds to a trade-off between the data fidelity term and the regularization term. Higher values of λ lead to more intense noise suppression in reconstructions. Correct estimation of variable s in Eq. (4) leads to compensating sample drifts that, in turn, results in better quality reconstruction. The proposed optimization problem is solved in [58] by using the alternating direction method of multipliers [62]. A GPU-accelerated implementation of the method is publicly available in the TomoAlign package.

A comparison between Gridrec and TomoAlign reconstructed slices is shown in Fig. S1. The final reconstructions are shown in Figs. 3(a-d), which display the same intermediate slice of the 3D reconstruction as a function of time (in hours).

2.3. Segmentation of eutectic phases

We faced another complication due to our decision to capture TXM scans at elevated temperature, which was the increased solubility of Ag in α -Al [26,35,44–46,48,50,63,64]. At 723 K, Ag can dissolve up to \sim 12wt% in α -Al before Ag₂Al starts to form (at equilibrium), compared to the <1wt%Ag solubility at room temperature (RT). Consequently, the Al phase, which is the least attenuating phase at RT, is now more attenuating than the Al₂Cu phase in subsequent *in situ* reconstructions at the anneal temperature. In addition, the Ag₂Al rods shrink in size and some dissolve completely into the Al matrix. Thus it is challenging to

apply a generic segmentation routine to partition the phases and track their evolution from the RT scan to those done at temperature.

To overcome this issue, we used a machine-learning based program, ZEN Intellesis developed by Carl Zeiss AG [65], which utilizes a neural network to classify each pixel in a designated image to one of three solid phases. We hand-segmented 20 randomly selected images, which were then used to train the model. Note that we needed two separate training sets to segment the as cast data (at RT) and those captured at elevated temperature. To verify our segmentations, we computed the average recall, precision, and F1-score [66,67] for each phase over all seven time steps. Each phase had an average score greater than 0.9 of 1 for all metrics, where 1 corresponds to a perfect segmentation. This confirms the high degree of reliability of the segmentation procedure. Refer to Appendix A for more details.

We also employed a watershed algorithm to improve the detection of the solid–solid interfaces, specifically those of the Al_2Cu phase. Then, the digitized interfaces of the eutectic solids were meshed (i.e., represented by a series of triangles and associated vertices). To remove any spurious staircasing artifacts, we smoothed the mesh by mean curvature flow [68]. We present our final 3D renderings of the evolving sample in Fig. 4 where the Al, Ag_2Al , and Al_2Cu phases are consistently depicted in green, red, and blue, respectively. Similar to Figs. 3, 4 shows the time-evolution of the microstructure over 4 hr.

2.4. Electron backscatter diffraction

Our next objective was to evaluate the crystal orientations of the eutectic phases as well as the orientation relationships between them. However, the as-cast microstructure of our TXM sample was no longer available. So, we obtained a fresh sample with the same composition and geometry as the original and recreated the growth conditions in DS. As expected, we found a similar pseudo-ladder three-phase

https://github.com/nikitinvv/tomoalign

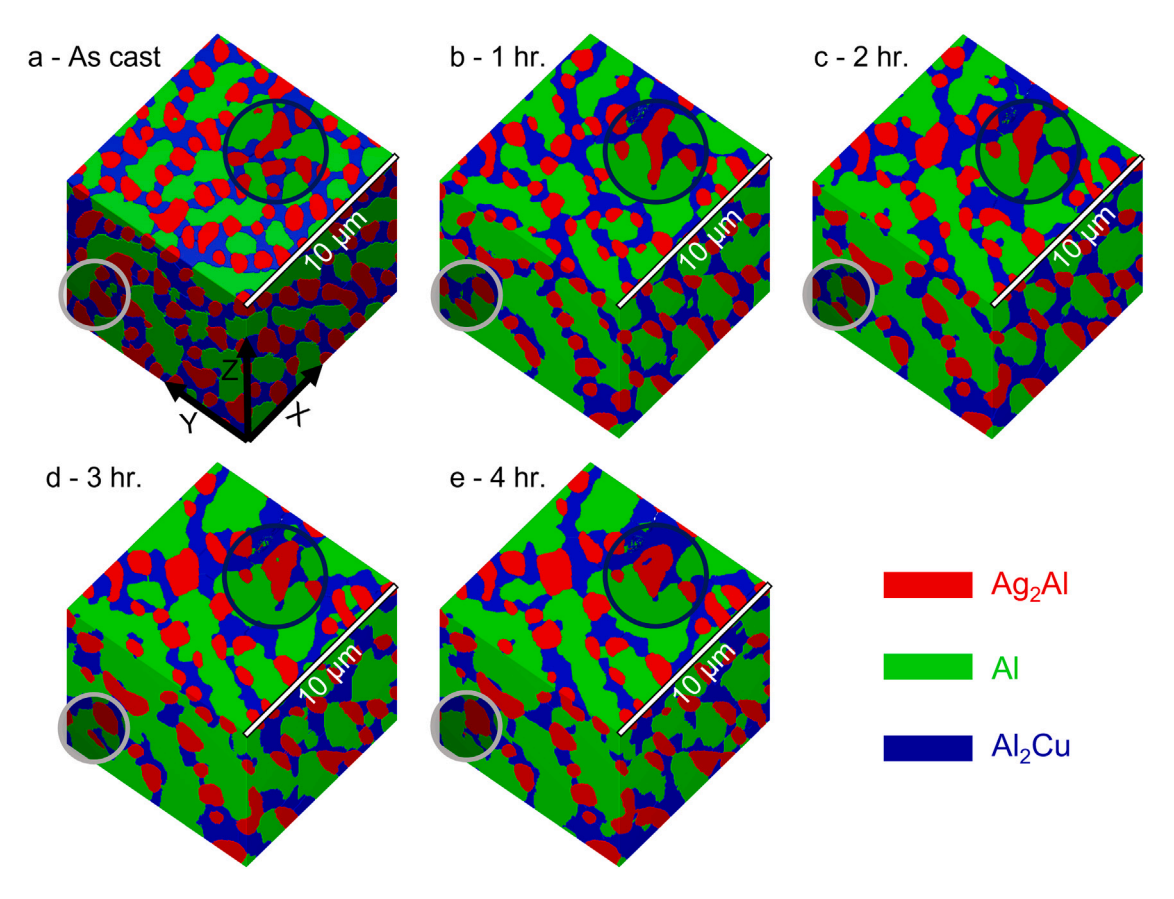


Fig. 4. A cubic subvolume of Al-Ag₂Al-Al₂Cu three-phase eutectic, annealed at 90% T_e (723 K). Data shown for a 0, b 1, c 2, d 3, and e 4 hr. Al, Ag₂Al, and Al₂Cu phases are designated in the colors green, red, and blue, respectively. The gray and black encircled regions highlight regions-of-interest within the evolving microstructure (see text). (For interpretation of the references to color in this figure legend, the reader is referred to the web version of this article.)

eutectic structure, which we then characterized *via* electron backscatter diffraction (EBSD). For this purpose, we polished the sample with 1200 grit paper and then reduced the surface roughness further with FIB. We captured Kikuchi patterns of a $23.5 \times 15.0 \ \mu m^2$ transversal region of as-solidified microstructure, nearly parallel to the thermal gradient G, using a $0.04 \ \mu m$ step size in a square grid.

Due to the unique mechanical properties of each phase and the $<5~\mu m$ lamellar spacing, we were not able to index the blurry Kikuchi patterns via traditional algorithms. Instead, we turned to dictionary indexing, which has demonstrated robustness against noise [69]. In short, the backscatter electron yield is simulated for a hypothetical single crystal of a specific phase viewed in a geometrical model of our sample-detector configuration. The simulated and experimental patterns are then transformed into Rodrigues–Frank vectors in the fundamental zone. Finally, a dot product of the two vectors is taken and a similarity metric is computed. The simulated pattern most similar to the actual is identified as the crystal orientation [69]. This automated procedure allowed us to index our EBSD data. We used MTEX open source software [70] in the Matlab [71] computing environment to process the indexed data and visualize the crystallographic information for each phase (vide~infra).

2.5. Combining TXM and EBSD data

To determine the crystallographic orientations of the solid–solid interfaces during the coarsening process, we must align the TXM and EBSD frames-of-reference, as a first step. Since we conducted TXM and EBSD scans on two *different* samples, it is nontrivial to register features in one dataset with those in the other. A second confounding issue is that the Ag_2Al rods are tilted 30° with respect to the thermal gradient (taken as the specimen *z*-axis); meanwhile, it is impossible to identify

the angle and direction of any similar tilt within the 2D transversal section imaged by EBSD.

To circumvent these issues, we must make two simplifying assumptions to align the data sets: Firstly, we assume that G in both samples is identical and parallel to the specimen z-axis, which is itself antiparallel to gravity. This assumption is based on the fact that both samples were solidified under identical conditions and held in-place in alumina crucibles, which prevented any macroscopic specimen tilt during DS. Secondly, we assume that the Al_2Cu growth direction is [001], which is also parallel to G and therefore z. This assumption is supported by several past studies [25,26,44,46,49,72], which altogether demonstrate that within the $Al-Ag_2Al-Al_2Cu$ eutectic, Al_2Cu grows in the [001] direction, regardless of its incipient growth morphology. With these assumptions in hand, we reoriented our tomography specimen into the EBSD frame-of-reference, as shown visually in Fig. 5(a-b).

To transform the interfacial orientations from the EBSD specimen to the crystallographic frame-of-reference, we follow the procedure outlined in Refs. [73,74]. We begin by computing local orientations (normal vectors) along patches of solid–solid interface, in the specimen frame. By convention, the normal vectors with respect to a given solid phase point outward, *i.e.*, towards its neighbors. The interface unit normal, \hat{n}_i , of mesh triangle i is given as

$$\hat{n}_{i,s} = \frac{\vec{e}_{i,1} \times \vec{e}_{i,2}}{\|\vec{e}_{i,1} \times \vec{e}_{i,2}\|}$$
 (5)

where $\vec{e}_{i,1}$ and $\vec{e}_{i,2}$ are the edge vectors or triangle i, measured in the specimen s frame.

To convert the normals in Eq. (5) from specimen coordinates, C_S , into crystallographic coordinates, C_C , we must specify a rotation matrix, g, such that $C_C = gC_S$ [75]. Each eutectic phase requires a single, unique g matrix (retrieved from EBSD), assuming the phases are single

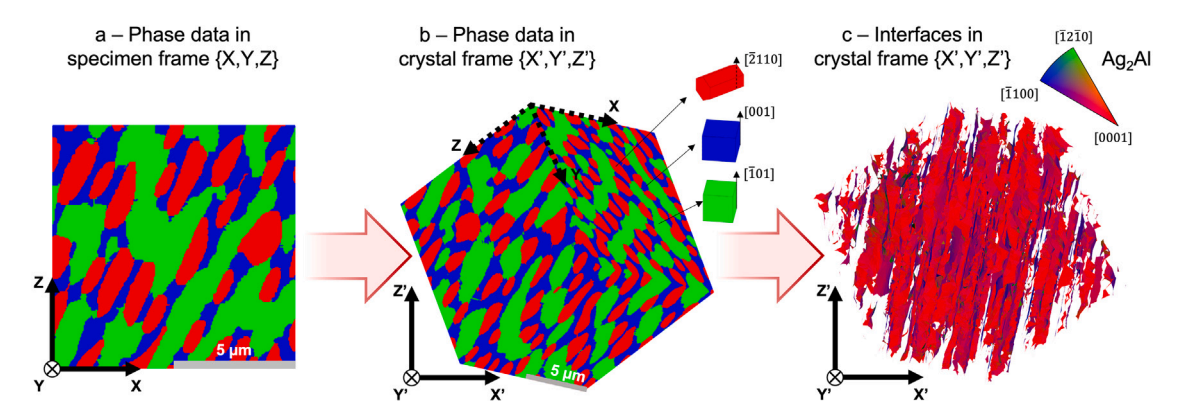


Fig. 5. Reorientation of reconstructed TXM volume into the crystallographic frame and computation of the Ag_2Al -Al and Ag_2Al -Al_2Cu bilateral common planes. In **a**, the original specimen frame-of-reference is shown with the eutectic phase data, as depicted in Fig. 4(b), where again Al, Ag_2Al , and Al_2Cu are in green, red, and blue, respectively. In **b**, the phase data is rotated to align with the EBSD map presented in Fig. 9. In **c**, the crystallographic orientations of Ag_2Al rods are displayed (referenced to the Ag_2Al frame, see standard triangle). (For interpretation of the references to color in this figure legend, the reader is referred to the web version of this article.)

crystals (proved later). Furthermore, for each crystal structure, such as face-centered cubic, hexagonal, and tetragonal for Al, Ag₂Al, and Al₂Cu, respectively, there is a set of point group symmetry operators, T_j . These operators represent the 48, 24, and 16 symmetry elements for 432, 6/mmm, and 4/mmm, respectively. Since Ag₂Al is hexagonal, we converted its indices to an orthonormal coordinate system, following Ref. [76]. Ultimately, we obtain all crystallographically-related solutions of the interfacial orientation, $\hat{n}_{i,c}$, as

$$\hat{n}_{i,c} = T_j g \hat{n}_{i,s} \tag{6}$$

This transformation is shown visually for the Ag_2Al phase in Fig. 5(c). After obtaining $\hat{n}_{i,c}$ for all mesh triangles and all phases, we display the results on a stereographic projection (inverse pole figure), hereby referred to as a crystallographic interface normal distribution (CIND) [6,73]. For interfaces between phases α and β , the CIND gives the probability of finding a given crystallographic orientation $\hat{n}_{i,c}$ (measured with respect to either α or β). Due to crystal symmetry, we restrict the CIND to the fundamental zone. By plotting CINDs as a function of time (holding g fixed for each phase throughout the anneal), we can track the development of preferred interfacial orientations during coarsening.

3. Results and discussion

3.1. Interaction between Ag_2 Al and Al_2Cu

As mentioned in the introduction, the coarsening dynamics in multiphase, multi-component systems differs from their two-phase, binary counterpart. This is because the coarsening behavior of one phase can impact the others, depending on the solubilities and diffusivities according to Eq. (1) [31]. Thus, to determine the cross-phase interaction between Ag₂Al and Al₂Cu, we calculate $\Gamma_{\rm Ag_2Al,Al_2Cu}$ and $\Gamma_{\rm Al_2Cu,Ag_2Al}$ using the thermophysical parameters given in Table 1. We obtain $\Gamma_{\rm Ag_2Al,Al_2Cu} = -0.014(1)$ and $\Gamma_{\rm Al_2Cu,Ag_2Al} = -0.018(1)$. Since these values are well below unity, we can suppose that the two phases will coarsen independently of each other and can examine the evolution of each separately, for sake of simplicity.

Indeed, this analysis appeals to our need to organize complex information into smaller units. Yet the theory assumes that the two phases are embedded randomly in a matrix, and interact *only* through concentration fields in that matrix [31,32]. This assumption is reasonable if the two phases occupy minor volume fractions. Otherwise, we must consider the role of the initial microstructure, namely the spatial correlations [77] and topological arrangements [43,44] of phases. Below, we show that this effect cannot be fully neglected.

Table 1 Thermophysical parameters. We estimate the diffusivity D_i of component i in the Al matrix at T = 723 K using an Arrhenius relationship, $D_i = D_{ai} \exp(-Q_i/(RT))$.

Phase n	Ag ₂ Al	Al ₂ Cu	Reference	
$\Delta c_{\text{Ag}}^{\alpha\text{-Al},n}$ (at%)	0.039(7)	-0.55(1)	TCAL8 [78]	
$\Delta c_{\mathrm{Cu}}^{\alpha\text{-Al},n}$ (at%)	-0.31(1)	-0.013(1)	TCAL8 [78]	
Component i	Ag	Cu	Reference	
$D_{o,i}$ (m ² /s)	1.18×10^{-5}	6.47×10^{-5}	[79]	
Q_i (kJ/mol)	116 ± 0.594	135 ± 1.13	[79]	

3.2. Evolution of Ag₂Al morphology

Initial condition. In Fig. 4, we examine the reconstructed volumes and focus on the Ag_2Al phase (shown in red). This phase is comprised of long fibers tilted at 30° with respect to the z-axis (parallel to G). In the as-cast state at RT, the eutectic pattern can be described as single rods [3,44,45]. The two intermetallic phases (Ag_2Al and Al_2Cu) alternate back-and-forth within narrow channels in the Al matrix. Yet unlike a regular ladder structure [43,46,72], in this case, Al_2Cu partially or completely encases several Ag_2Al rods. As such, Al_2Cu forms an interconnected, bicontinuous structure rather than discrete rods in

Time evolution. In Fig. 4(b), we observe the dissolution of Ag_2Al rods into the Al matrix, as we bring the sample from RT to 723 K. Consequently, the entire eutectic pattern undergoes a realignment of Ag_2Al - Al_2Cu chains, as small rods of Ag_2Al disappear. The Al_2Cu phase does not undergo a similar change in volume fraction, resulting in a complete encasement of the newly shrunken Ag_2Al rods by Al_2Cu . Dissolution of Ag_2Al is rapid and has long-lasting effects on the eutectic microstructure. Even so, after the 1-h mark, the newly established volume fractions remain relatively stable for the rest of the anneal.

As coarsening progresses, smaller Ag_2Al rods gradually disappear while adjacent rods grow in size. One example can be seen in the gray circled region of Fig. 4. Here, two of the initial three Ag_2Al rods disappear over time-steps (a-e), while the third rod is growing at its neighbors' expense. Meanwhile, in the black circled region, we see three separate rods in (a) that coalesce in (b) to form an irregularly shaped rod. During (c-e), we see the elongated structure undergo curvature reduction and become much less peninsular. By virtue of the 3D data, we do not identify any faults along the Ag_2Al rods, which are characterized by pairs of terminations and branches. Moreover, we see no evidence of discontinuous coarsening [19].

Kinetics of rod growth. To determine the operative coarsening mechanism, we used the PolyProc function package [80] to assign order parameters to all discrete rods in the reconstructed volume, and track

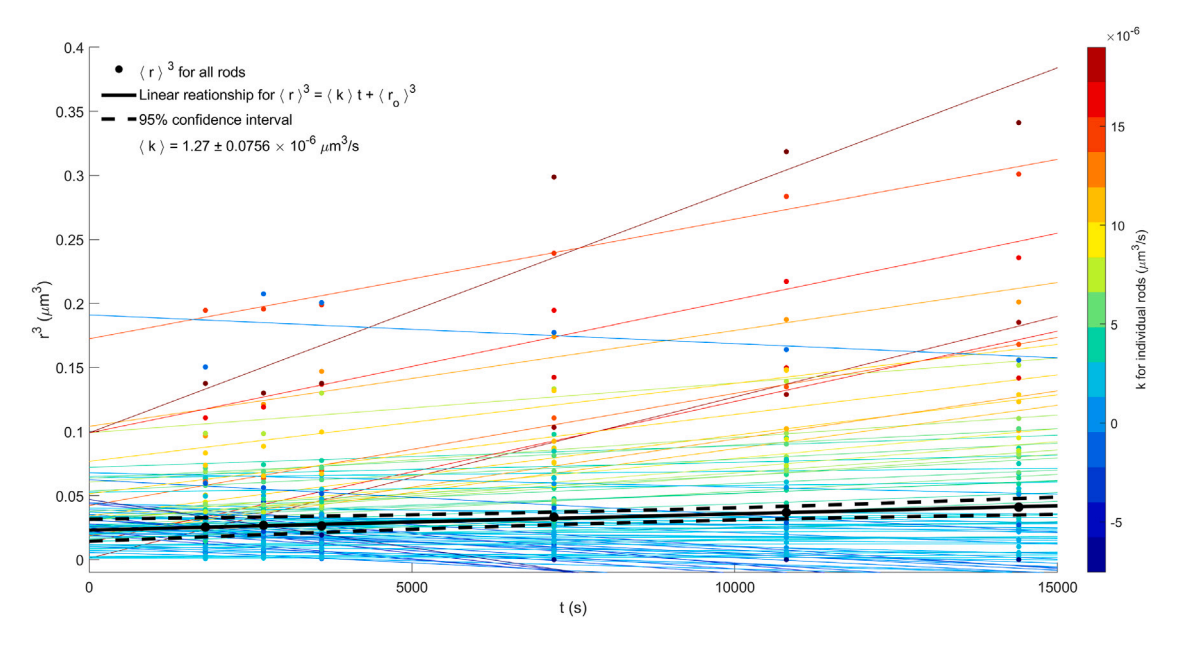


Fig. 6. *Dynamic scaling of* Ag_2Al *rods*, on a plot of radius cubed, r^3 , vs. time, t, for all individually tracked rods. The discrete data points and corresponding linear fits are color-coded according to the computed rate constant, k, see color-bar. The average dynamics and corresponding 95% confidence interval is conveyed in black with a slope given by $\langle k \rangle$, indicated in the upper left-hand corner. (For interpretation of the references to color in this figure legend, the reader is referred to the web version of this article.)

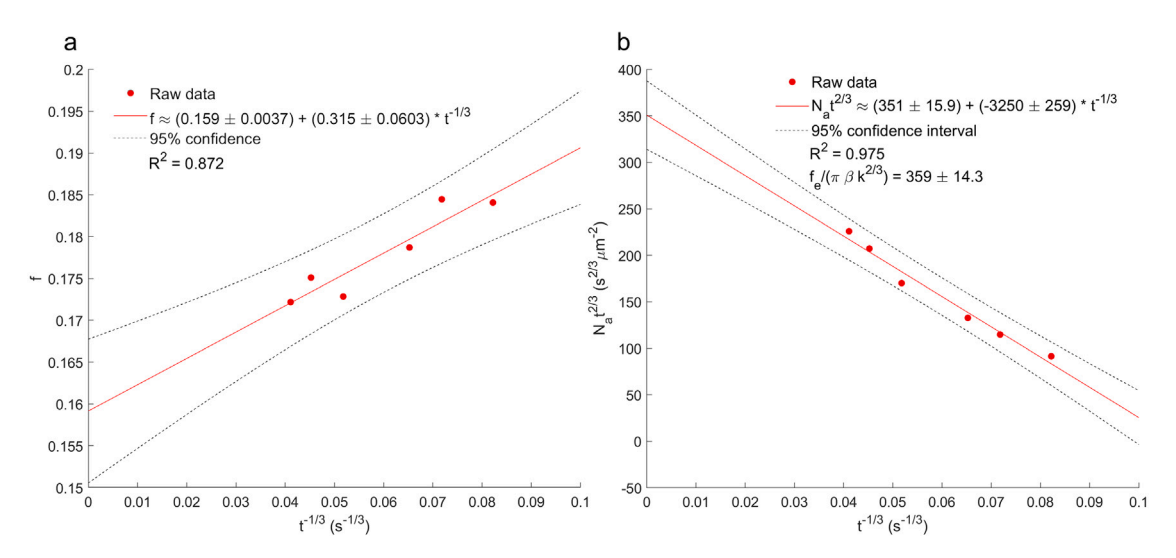


Fig. 7. Consistency checks: a volume fraction of Ag_2AI , f, and \mathbf{b} number of Ag_2AI rods per unit area, N_a , vs. inverse cube root of time, $t^{-1/3}$, cf. Eq. (8). Both plots also indicate their respective 95% confidence intervals. The linear relationships are given in the upper left-hand corner of each plot.

the evolution of each rod across multiple time steps. We computed the equivalent radius r for every identified rod over six time steps t at 723 K; of course, some rods were consumed within the 4-h experiment. For the coarsening of fibers with a cylindrical geometry (i.e., 2D Ostwald ripening), it can be shown [19,81] that

$$r^3 - r_o^3 = kt \tag{7}$$

where k is the rate constant for coarsening and r_o is the radius at the onset of steady-state ripening. Assuming the relevance of Eq. (7), we plot in Fig. 6 the radius cubed, r^3 , *versus* time, t, for each rod. We color the corresponding $\{r,t\}$ datasets by k. The average coarsening rate for all the rods, $\langle k \rangle$, was found to be $1.27 \pm 0.0756 \times 10^{-6}~\mu\text{m}^3/\text{s}$. This rate constant is notably lower than that reported by Ref. [82] for Ag₂Al precipitates in a *binary* Al-10 wt% Ag alloy at 473 K, $k = 8 \times 10^{-4}~\mu\text{m}^3/\text{s}$, which would suggest a non-negligible influence of Al₂Cu on the coarsening dynamics of Ag₂Al. A closer inspection of the data reveals that many rods have a negative r^3 value at later time-steps since they

disappear before the final time-step. In addition, rods with negative k values are shrinking in time. In contrast, other rods appear to have little to no change in r during coarsening, while eleven Ag₂Al rods display a dramatic increase in size with $k > 1 \times 10^{-5} \ \mu \text{m}^3/\text{s}$.

As a robustness check, we estimate from our data the equilibrium volume fraction of Ag₂Al, f_e , noting that the instantaneous volume fraction f should decay slightly with time t [83]. Thus, we plot f against $t^{-1/3}$, see Fig. 7(a). By extrapolating the data to $t \to \infty$, we obtain $f_e = 0.159 \pm 0.0037$. Notably, this value is very close to $f_e = 0.16$ reported by Ref. [43] for an alloy of equivalent composition.

Kinetics of rod evanescence. As a system undergoes 2D Ostwald ripening, the number of rods or fibers per unit area, N_A , decreases with time, t, as

$$N_A \approx \frac{f_e}{\pi \beta k^{2/3}} t^{-2/3} - \frac{(1 - f_e)l}{\langle u \rangle \pi \beta \Delta c_e k} t^{-1}$$
 (8)

where β is $\frac{\langle r \rangle^2}{\langle r^2 \rangle}$, l is the capillary length, $\langle u \rangle$ is $\frac{r}{\langle r \rangle}$ in Lifshitz–Slyozov–Wagner theory [84,85] and Δc_e is the equilibrium solubility of the

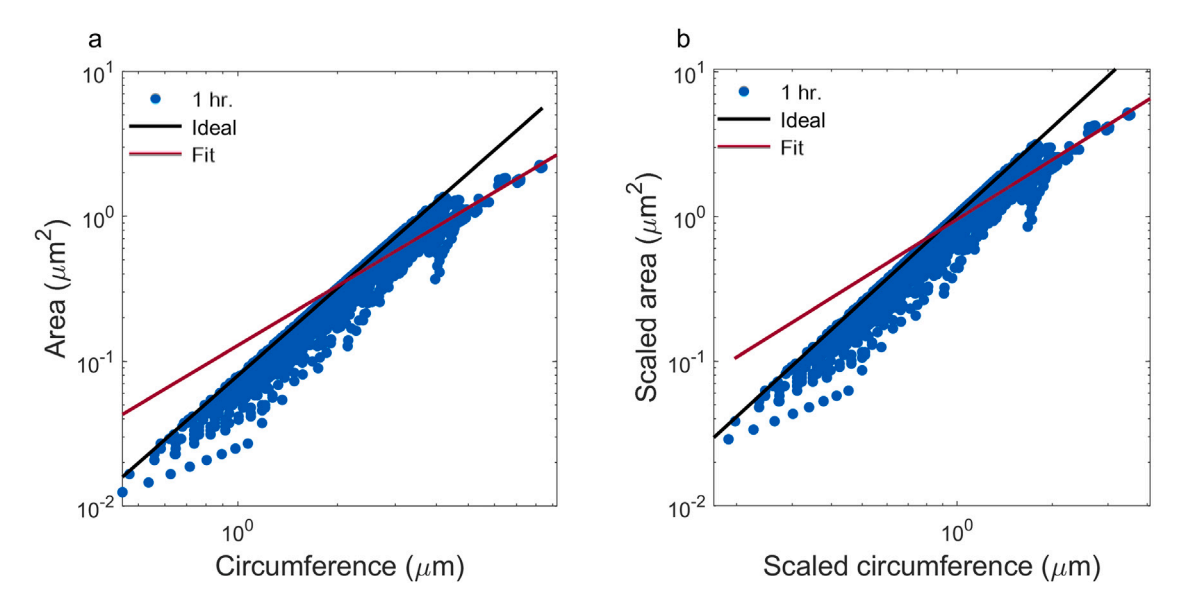


Fig. 8. Morphology of Ag₂Al rods: log-log plots of **a** area vs. circumference and **b** scaled area vs. scaled circumference of domains captured after 1 hr. of annealing. The 'ideal' case (circular cross-sections) is shown in black and the fit to the last 50 data-points is shown in red.

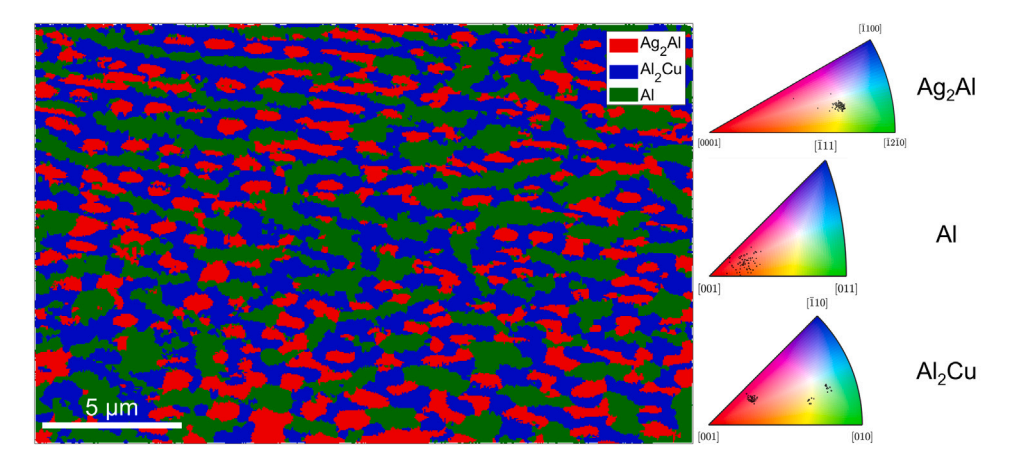


Fig. 9. EBSD phase map of as-cast Al-Ag₂Al-Al₂Cu three-phase eutectic, solidified at $G \approx 1.5$ K/mm and $\frac{dT}{dt} \approx 0.9$ K/min. Al, Ag₂Al, and Al₂Cu phases are depicted in green, red, and blue, respectively. Inverse pole figure for each phase shown at right. (For interpretation of the references to color in this figure legend, the reader is referred to the web version of this article.)

dispersed phase. With Eq. (8) in mind, we plot $N_A t^{2/3}$ vs. $t^{-1/3}$, see Fig. 7(b). The y-intercept gives $\frac{f_e}{\pi \beta k^{2/3}}$, which we find to be 351 ± 15.9 s^{-2/3} μ m⁻². Using $f_e = 0.16$ from Ref. [43], $\langle k \rangle$ from Fig. 6, and calculating β using the list of r at t=4 h, we directly compute $\frac{f_e}{\pi \beta k^{-2/3}}$ as 359 ± 14.3 s^{-2/3} μ m⁻². The extrapolated and computed values agree within 1%, and it is this self-consistency between the parameters in Eqs. (7)–(8) that indicates the Ag₂Al phase evolves via 2D Ostwald ripening.

At first glance, the conformation of our data to the scaling relations may appear somewhat surprising. This is because power law scaling implies the presence of a self-similar microstructure [86]. Instead, we observe that several Ag_2Al rods changed shape and developed faceted features with long, flat interphase boundaries; we also observe several Ag_2Al rods coalesce with neighboring rods, as mentioned previously. Nevertheless, the scaling relations are robustly observed in many other systems *without* a self-similar morphology, for example, at high volume fractions in a binary system (where coalescence is inevitable) [87].

Rod coalescence. To understand the effect of coalescence on the interfacial morphology, we collected the area-to-circumference ratios in 2D sections for all Ag_2Al rods at the 1 hr. mark. See Fig. 8(a). The black line indicates the 'ideal' relationship between area and circumference if the domains would be circular in cross-section. Clearly, the largest domains display the lowest area-to-circumference ratio, deviating from

the ideal (see red trend-line) and hence corresponding to coalescence events. Following Ref. [29], in Fig. 8(b) we scaled the axes by the mean area and mean circumference. From this data it can be seen that the black and red lines intersect around the mean values, indicating that the domains with radii larger than $\sim 1\times$ the equivalent mean radius are most likely to coalesce.

3.3. Evolution of Al_2 Cu morphology

Graham and Kraft [88] reported that the lamellar eutectic Al-Al $_2$ Cu evolves through fault migration. According to Weatherly [89], these fault lines correspond to subgrain boundaries. However, it is uncertain if fault migration is necessarily responsible for coarsening of Al $_2$ Cu within a three-phase eutectic microstructure. As a first step to understanding the morphological evolution of Al $_2$ Cu, we examine the crystallography of the system. Fig. 9 shows a phase map of the three-phase eutectic with corresponding inverse pole figures (IPF) for each phase. We observe that data for Al $_2$ Cu are densely packed into three regions, with the cluster of data-points nearest to $\{001\}$ accounting for the majority of orientations. The low orientation spread (within 2°) indicates that Al $_2$ Cu has a low incidence of subgrain boundaries, and hence a low fault density, *i.e.*, it is a single crystal.

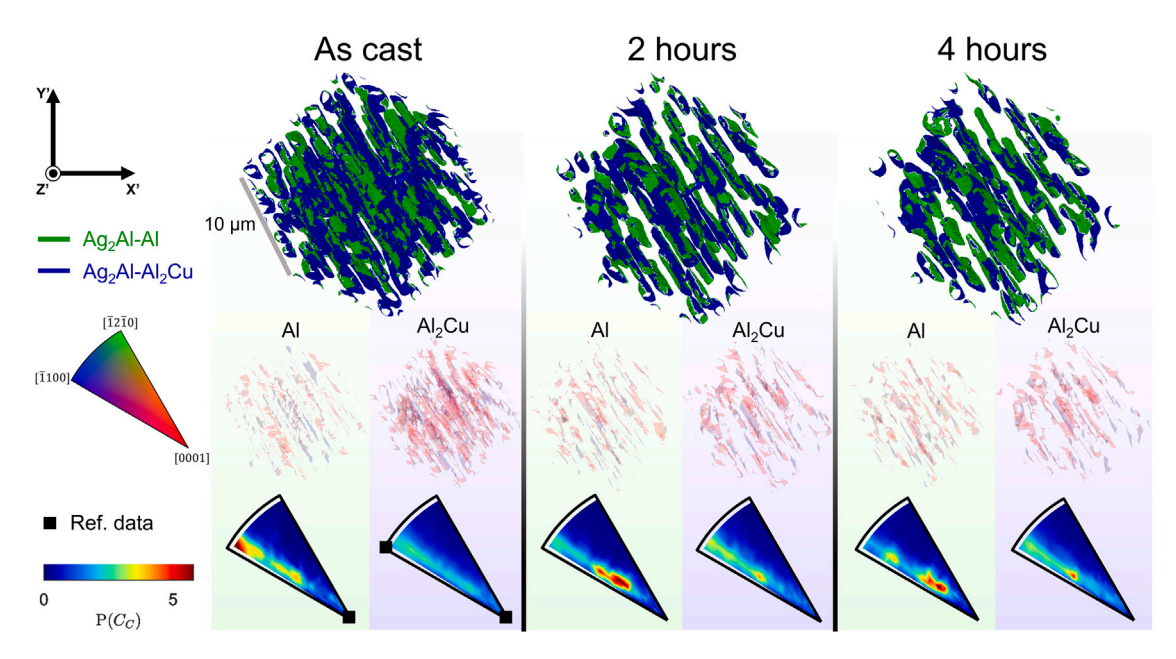


Fig. 10. Coarsening evolution of all Ag_2Al-Al_2Cu and Ag_2Al-Al interphase boundaries, shown over three time steps: 0, 2, and 4 hours. The top row displays Ag_2Al rods colored according to the interphase boundary type, where green is Ag_2Al-Al and blue is Ag_2Al-Al_2Cu . The middle row shows interphase boundaries for Ag_2Al-Al (left) and Ag_2Al-Al_2Cu (right). Each interfacial patch is illuminated according to its crystallographic orientation within the standard triangle at left. The bottom row gives corresponding CIND plots in the Ag_2Al frame. All plots have been scaled to the same color-bar limits to facilitate comparison between them. Black squares identify the habit plane orientations reported in Ref. [47], namely $(000\overline{1})_{Ag_2Al}$ and $(1\overline{100})_{Ag_2Al}$. (For interpretation of the references to color in this figure legend, the reader is referred to the web version of this article.)

In the absence of faults, it remains to be determined how $\mathrm{Al_2Cu}$ coarsens. Unlike $\mathrm{Ag_2Al}$, identifying the underlying mechanism for $\mathrm{Al_2Cu}$ is somewhat challenging since it does not show an equiaxed shape. In Fig. 4, it can be seen that $\mathrm{Al_2Cu}$ is highly interconnected and forms a pseudo-ladder structure. For this reason, we replace r in Eq. (7) with the inverse surface area per unit volume S_v^{-1} as an appropriate length-scale [90,91], see Fig. S2. Since $S_v^{-1} \propto t^{1/3}$ asymptotically, $\mathrm{Al_2Cu}$ coarsens via 3D Ostwald ripening.

3.4. Evolution of interfacial bicrystallography

The lack of self-similarity from the above analysis (particularly for Ag_2Al) raises important questions about the changes in interfacial crystallography over time and how they relate to morphological changes. Given the preferential crystal orientations for Al, Ag_2Al , and Al_2Cu (cf. Fig. 9), we can determine not only the orientation relationships of the three phases, but also the common planes (CPs) of their interphase boundaries (so-called bilateral CPs).

Orientation relationships. From the EBSD data of the as-cast microstructure, we determine the epitaxial relations: we identify the common directions as $[\bar{1}01]_{Al} \parallel [\bar{2}110]_{Ag_2Al} \parallel [001]_{Al_2Cu}$, and the common planes as $(\bar{1}3\bar{1})_{Al} \parallel (01\bar{1}0)_{Ag_2Al} \parallel (110)_{Al_2Cu}$. By transforming the TXM data to the crystallographic frame (see Section 2.5), we find the bilateral CP between the two intermetallics (Fig. S3a-c) in the RT data as $(0001)_{Ag_2Al} \parallel (\bar{1}10)_{Al_2Cu}$. Similar ORs for this three-phase eutectic have been reported elsewhere [47,49,72]. Additionally, EBSD data was collected from another region of the sample, coarsened for 4 hr. The OR does not change with time (Fig. S3d-f), indicating there is no grain rotation.

Interfaces of Ag_2Al . We calculated the crystallographic normals ($\hat{n}_{i,c}$ in Eq. (6)) along all solid–solid interfaces over the course of the anneal, beginning with those bounding the Ag_2Al phase. Fig. 10 illustrates the time-evolution of the bilateral CPs for the ensemble of Ag_2Al rods at three representative time steps. In the top row, we distinguish between Ag_2Al -Al and Ag_2Al -Al $_2$ Cu boundaries in green and blue, respectively. The middle row displays the same solid–solid interfaces such that each patch of interface is colored according to its local orientation, see the

standard triangle at left. In the bottom row, we provide the corresponding CIND for each interphase boundary. The color-bar limits are fixed throughout to allow for comparison. Similar to past reports by Ref. [47] and others (black points), there is a relatively high probability of finding Ag_2Al -Al and Ag_2Al -Al $_2$ Cu aligned to the basal plane, prismatic plane, or both in its as-cast state. However, upon annealing, the rods appear to evolve into less frequently reported interfacial orientations (e.g., Ag_2Al -Al $_2$ Cu approaches $\{\bar{2}203\}$ after 4 h). This suggests that the reported bilateral CPs of $\{0001\}$ and $\{\bar{1}100\}$ may not necessarily be the lowest energy interphase orientations.

To disaggregate the above statistics, we focus on a small subset of Ag_2Al rods and tracked their development over 4 h, see Fig. 11. The top row shows a classification of interphase boundaries, the middle row the crystallographic orientation of each boundary referenced to Ag_2Al , and the bottom row the corresponding CINDs normalized to the same range. We notice in the top row that the Ag_2Al rods coalesced over time. At the 2 hr. mark, the center and right rods completely fused into a single misshapen rod. Additionally, we observe the beginning of a similar coalescence event involving the center and leftmost rod. Note that the Ag_2Al rods were separated by a narrow ~250 nm thick region of Al_2Cu . Thus the coalescence of Ag_2Al could only take place because of the elimination of the Al_2Cu phase, i.e., the consolidation of one phase is the direct consequence of the evolution of the other.

According to the bottom row of Fig. 11, the bilateral CPs of Ag_2Al align with $\{0001\}$ and $\{\bar{1}100\}$ in the as-solidified structure, consistent with past reports [47]. After the first hour, these planes continue to dominate the CIND. However, after 2 hr. (when coalescence begins), the distribution of interfacial orientations is markedly different: the most probable orientation of the Ag_2Al-Al_2Cu boundary shifts to $\{0001\}$, while the Ag_2Al-Al boundary moves to $\{\bar{2}203\}$. This shift occurs in less than 2 hr. before the interfaces appear to 'lock' into the faceted, convex structure seen at the end-state. On closer inspection, we notice that the rods coalesce along $\{\bar{1}100\}$ boundary with Al_2Cu , which explains why this orientation becomes less probable in comparison to $\{0001\}$. We can also compare the $\{\bar{2}203\}$ plane against that of other studies. For example, $\{\bar{2}203\}$ differs by 10.7° from the $\{\bar{1}101\}$ plane reported by Friess et al. [49]. Therefore, it is not unreasonable that Ag_2Al displays these interfaces before locking in place. In the case of

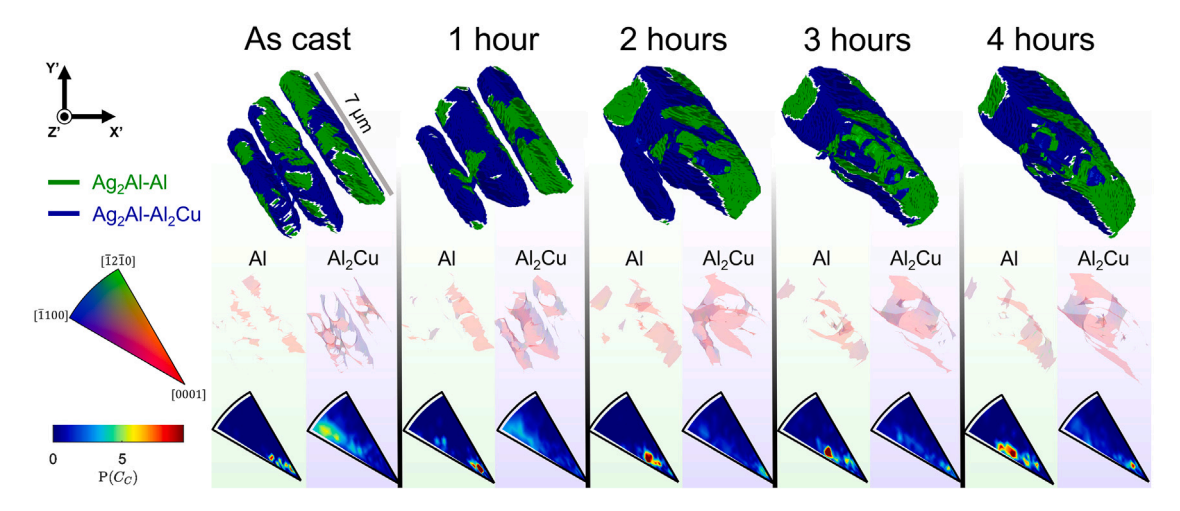


Fig. 11. Coarsening evolution of three adjacent Ag_2Al rods which coalesce into a single domain. Ag_2Al - Al_2Cu and Ag_2Al -Al interphase boundaries are shown over five time steps: 0, 1, 2, 3, and 4 hr. The top row shows the isolated Ag_2Al rods colored according to the interphase boundary type, where green is Ag_2Al -Al and blue is Ag_2Al -Al (left) and Ag_2Al -Al₂Cu (right), where interfacial patches are illuminated according to their crystallographic orientation within the standard triangle at left. The bottom row displays corresponding CIND plots in the Ag_2Al frame. All plots have been scaled to the same color-bar limits to facilitate comparison between them. (For interpretation of the references to color in this figure legend, the reader is referred to the web version of this article.)

the Ag_2Al -Al boundary, we observe that the peak in the CIND value has shifted by 35.4°, but we have no information about the kinetics that led to this transformation, only the final product.

To quantify the above behavior, we calculate the area fractions that belong to each interphase boundary as a function of time. Fig. S4(a) illustrates the evolution of the Ag_2Al -Al boundary and indicates a 53% reduction in {0001} planes and a 49% increase in $\{\bar{2}203\}$ planes. The rate of change of the area fractions drops quickly after 2 hr. of coarsening. In Fig. S4(b), we observe the transformation of the Ag_2Al -Al $_2$ Cu boundary, where we again see rapidly changing area fractions before stagnating after the 2 hr. mark.

Interfaces of Al and Al2Cu. Figs. S5-S6 illustrate the changes in morphology and interfacial orientation of Al₂Cu and Al phases in the same, bulk volume as in Fig. 10. We also give a similar set of plots for the smaller field-of-view as in Fig. 11, see Figs. S7-S8. According to the CINDs therein, the Al₂Cu-Ag₂Al interface has a slight preference for {110} (referenced to the Al₂Cu crystal) in the as-cast state and evolves to {130} during coarsening. In contrast, the Al-Ag₂Al interphase boundaries do not show a clear progression (when referenced to the Al crystal), starting near $\{\overline{1}22\}$ and then shifting towards $\{011\}$ before moving towards $\{\overline{1}11\}$ in the later stages of coarsening. It is possible that this evolution is part of a larger change that reduces the overall interfacial energy, but this will be proved later in Section 3.5. Taken altogether, the coalescing Ag₂Al rods initially have the bilateral CPs $\{0001\}_{Ag_2Al} \parallel \{\overline{122}\}_{Al} \text{ and } \{\overline{11}00\}_{Ag_2Al} \parallel \{\overline{11}0\}_{Al_2Cu}, \text{ which give way } \{0001\}_{Ag_2Al} \parallel \{\overline{122}\}_{Al} = \{0001\}_{Ag_2Al} = \{00$ to $\{\overline{2203}\}_{Ag_2Al} \parallel \{\overline{111}\}_{Al}$ and $\{0001\}_{Ag_2Al} \parallel \{\overline{113}\}_{Al_2Cu}$ over the 4 hr. anneal.

3.5. Selection of interfaces during coarsening

To understand why certain orientations dominate as time proceeds, we compute and compare the lattice misfits for the different interphase boundaries from above. Since the interfaces are semicoherent [35,47,92], the orientations with the lowest misfits should correspond to the lowest interfacial energies, neglecting thermal and chemical effects. Misfit, δ , is found as

$$\delta = 2 \frac{\|\rho_{\gamma} - \rho_{\beta}\|}{(\rho_{\gamma} + \rho_{\beta})} \tag{9}$$

where ρ_i represents the atomic density of phase i. In general, the atomic density of a lattice plane is expressed as $\rho = \frac{nd}{\Omega}$, where n is the number of atoms per unit cell in the plane, d is the interplane spacing, and Ω is the volume of the unit cell. However, this definition often leads

to varying ρ (and hence δ) since it requires the selection of a *specific* atomic layer. To overcome this limitation, we adopt the 'puckered' interface description [30,91], which calculates ρ by taking into account additional atoms that are slightly above and slightly below a given plane. This enables us to determine a minimum δ for a set of bilateral CPs

Fig. 12 shows the planar density ρ as a function of the thickness of a given layer wherein the 'puckered' atoms may be located. Each line represents the contribution of additional atoms to ρ . For each type of interphase boundary, the smallest difference in planar density for the same plane thickness give us the minimum lattice misfit. Table 2 summarizes the results for both the initial (as-cast) and final (4-h) states. It can be seen that the lattice misfits for both Ag₂Al-Al and Ag₂Al-Al₂Cu interfaces reduce over time, from 8.12% to 5.50% and 10.2% to 3.55%, respectively. This apparent shift suggests that coalescence drives the overall reduction in interfacial energy, for the field-of-view so considered. To lend credence to this idea, in Fig. 13 we plot the surface areas for $\{0001\}_{Ag_2Al}~\|~\{\overline{1}13\}_{Al_2Cu}$ (in blue) and $\{\overline{2}203\}_{Ag_2AI} \parallel \{\overline{1}11\}_{AI}$ (in green) vs. time, together with snapshots of the Ag₂Al rod cross-sections. The colors of the interfaces match the corresponding data-points. Clearly, consolidation of Ag₂Al leads to the expansion of the $\{0001\}_{Ag_2Al}$ interface with Al_2Cu and also a broadening of $\{\overline{2}203\}_{\mathrm{Ag_2Al}}$ with Al. We measure the dihedral angle ϕ between these two interfaces and find $\phi \sim 60.3^{\circ} \pm 13.9^{\circ}$; the actual interplanar angle of 51° between $\{0001\}_{Ag_2Al}$ and $\{\overline{2}203\}_{Ag_2Al}$ is clearly within this standard deviation. Since both Ag_2Al interfaces have comparable and low misfit, it follows that neither plane can expand further without sacrificing the other. As a result, the morphological evolution appears to stagnate, and the two planes 'lock' to form a faceted geometry at long times. The competition between the two interfaces may also explain why Ag₂Al never attains its equilibrium shape with Al (a hexagonal plate [82]), at least within the finite duration of our experiment.

We caution that the above puckering analysis provides only a preliminary assessment and does not consider the solubility of Ag in α -Al nor lattice expansion at elevated temperature. It will be necessary to carry out molecular dynamics simulations (akin to Ref. [93]) to determine the interphase boundary energies and correlate them to the experimental observations. In addition, the high index planes of Ag₂Al at the later time-steps may display a regular array of steps and kinks. Such an effect would only be visible through high resolution imaging techniques such as TEM. This is an avenue of current research.

In the future, we also intend to develop a clearer picture of the early-stage dynamics, during which fault migration may dominate coarsening [27]. Although we found limited faults along the Ag_2Al rods in

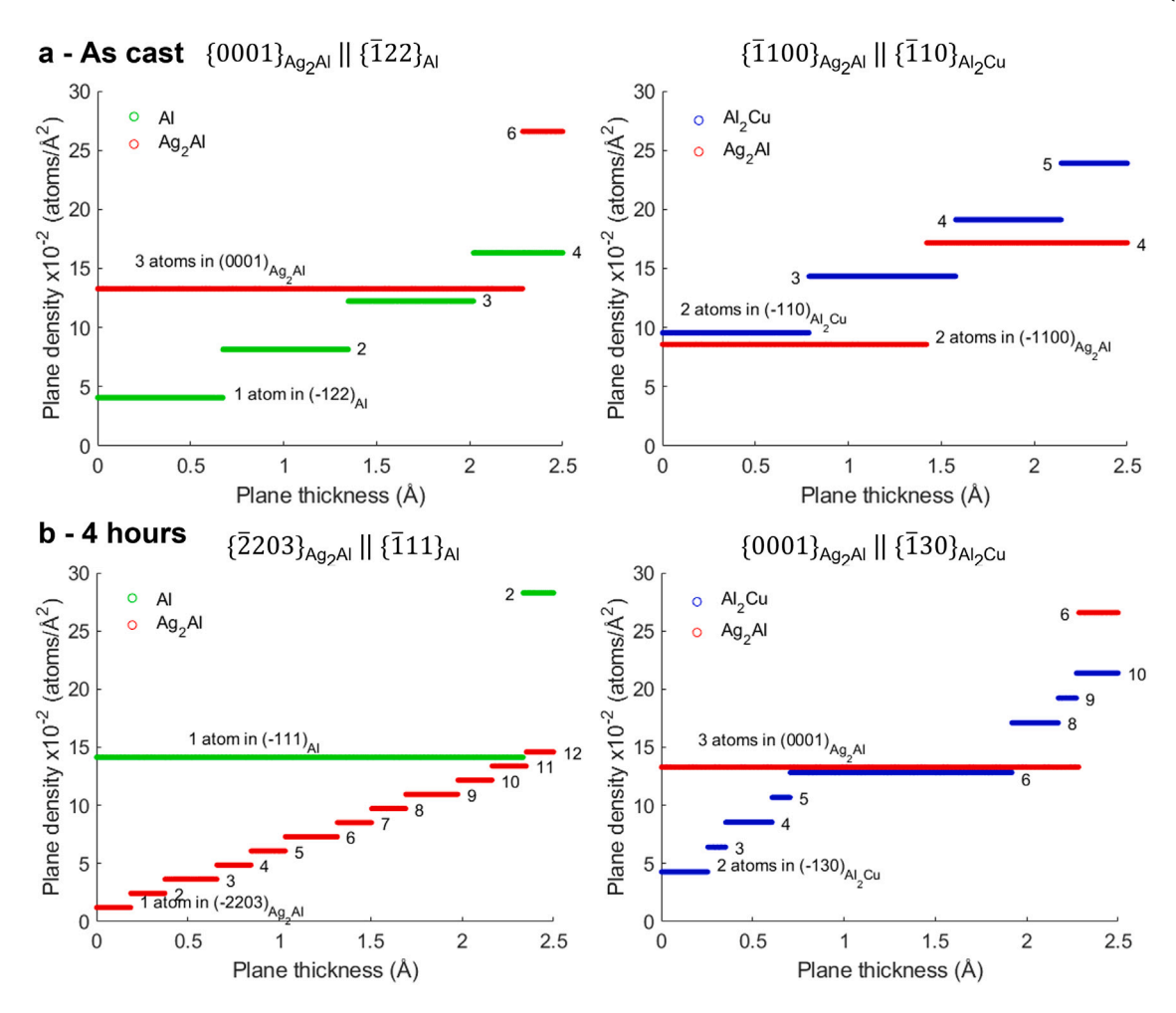


Fig. 12. Misfit of solid–solid interfaces. Computed planar density of different crystal orientations, considering all atoms within a certain atomic layer thickness (defined as the distance from the interface into the crystal of the listed phase). Accordingly, we compute the minimum misfit as the smallest difference in atomic planar density of the two solid phases. Using the orientations found for the isolated Ag₂Al rods in Fig. 11, a displays the planar density of the most prominent orientations in the as-cast state for the two types of hetero-interfaces: $\{0001\}_{Ag_2Al} \parallel \{\overline{1}22\}_{Al}$ and $\{\overline{1}100\}_{Ag_2Al} \parallel \{\overline{1}10\}_{Al_2Cu}$. b shows the planar densities of the most prominent orientations after 4 hr. of coarsening: $\{\overline{2}203\}_{Ag_2Al} \parallel \{\overline{1}11\}_{Al}$ and $\{0001\}_{Ag_2Al} \parallel \{\overline{1}30\}_{Al_2Cu}$. Al, Ag₂Al, and Al₂Cu are in green, red, and blue, respectively. (For interpretation of the references to color in this figure legend, the reader is referred to the web version of this article.)

 Table 2

 Interfacial bicrystallography, at initial and final time-points of the anneal process.

	As cast		4 hr.	4 hr.		
Interphase boundary	Ag ₂ Al Al	Ag₂Al ∥ Al₂Cu	Ag₂Al ∥ Al	Ag₂Al ∥ Al₂Cu		
Bilateral CPs	$\{0001\} \parallel \{\overline{1}22\}$	$\{\overline{1}100\} \parallel \{\overline{1}10\}$	$\{\overline{2}203\} \parallel \{\overline{1}11\}$	$\{0001\} \parallel \{\overline{1}30\}$		
Number of atoms in plane	3 3	2 2	11 1	3 6		
Planar density (atom/nm ²)	13.(3) 12.(3)	8.5(9) 9.5(6)	13.(4) 14.(1)	13.(3) 12.(8)		
Planar misfit (%)	8.12%	10.2%	5.50%	3.55%		

the as-cast structure, terminations and branches have been previously reported for the Ag_2Al phase [46], and therefore fault migration cannot be necessarily ruled out. Finally, we aim to investigate the influence of the initial condition: the Al- Ag_2Al - Al_2Cu three-phase eutectic produced several distinct patterns during DS [43,44,46,64,77], and the arrangement of phases and the ORs between them may impact the coarsening pathway.

4. Conclusions

We probed the coarsening dynamics of a model three-phase eutectic *via in situ* 4D X-ray nano-imaging coupled with EBSD. This investigation led to the following conclusions:

- We demonstrated a method to reconstruct X-ray micrographs corrupted by noise from thermal vibrations. Using TV-regularized reconstruction with deformation compensation and machine learning segmentation, we characterized the three eutectic phases and their respective interphase boundaries.
- Based on this data, we found that two of the phases (Ag₂Al and Al₂Cu) obey a temporal power law for their average length-scales, matching the predictions of theory. Even so, the eutectic microstructures are *not* self-similar in time.
- One reason for the absence of self-similarity is the coalescence of neighboring Ag₂Al rods, which involves the elimination of an intervening Al₂Cu channel. This demonstrates that the coarsening of one phase (Ag₂Al) is limited by the other (Al₂Cu), in a multi-phase system with comparable volume fractions.
- By correlating our absorption and diffraction data, we identified the common planes at the solid-solid interfaces. In this way, we

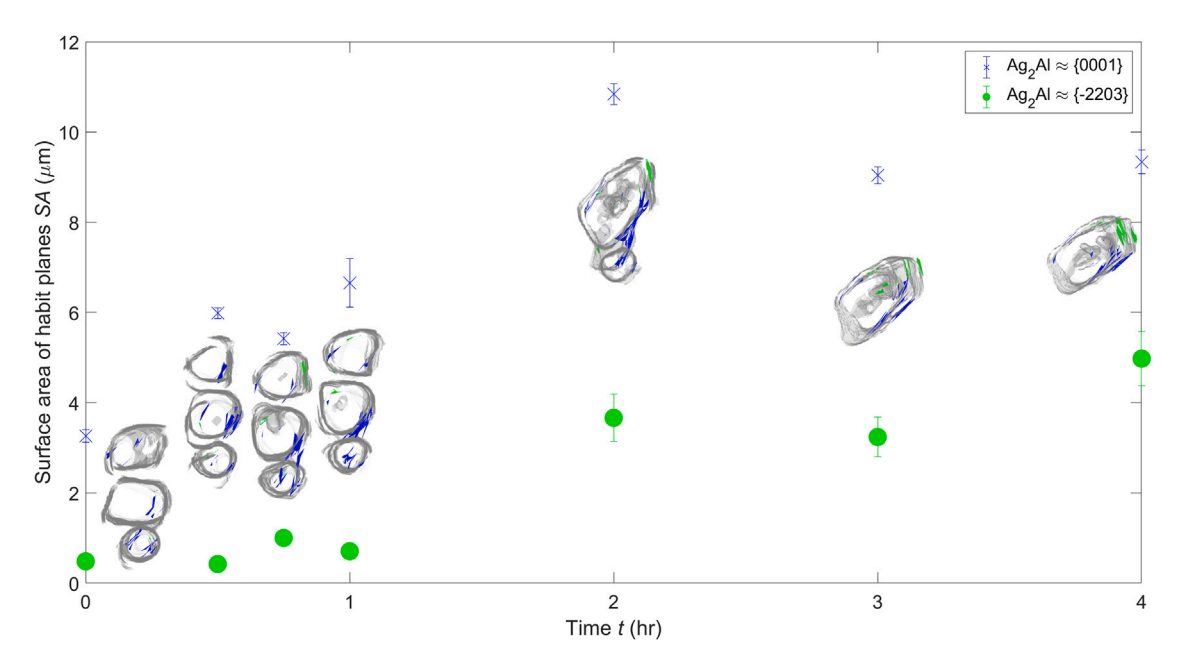


Fig. 13. Evolving surface area of Ag_2Al interfaces. Surface area of $\{\bar{2}203\}_{Ag_2Al}$ and $\{0001\}_{Ag_2Al}$ habit planes vs. time. A 3D mesh of Ag_2Al rod surfaces at each time step is shown inset, in gray, viewed along the long axis of the rods. Planes which align with $\{\bar{2}203\}_{Ag_2Al}$ and $\{0001\}_{Ag_2Al}$ have been colored to match the data points. For display purposes only, the Ag_2Al rod mesh is pre-processed to prevent any gaps from smoothing. This leads to a small misalignment between the mesh and the labeled habit planes.

determined that coalescence leads to a selection of interfaces that possess low misfit, and by extension, low energy.

Declaration of competing interest

The authors declare that they have no known competing financial interests or personal relationships that could have appeared to influence the work reported in this paper.

Declaration of Generative AI and AI-assisted technologies in the writing process

During the preparation of this work the authors used ChatGPT [94] in order to improve cohesion and clarity of the text. After using this tool, the authors reviewed and edited the content as needed and takes full responsibility for the content of the publication.

Acknowledgments

We thank the Air Force Office of Scientific Research under awards FA9550-18-1-0044 and FA9550-21-1-0260. We also thank Dr. Insung Han for his assistance in the acquisition of the TXM data. We thank the Michigan Center for Materials Characterization for use of the instruments and staff assistance. Marc De Graef would like to acknowledge financial support from the National Science Foundation (grant DMR-2203378) as well as the use of the computational resources of the Materials Characterization Facility at Carnegie Mellon University supported by grant MCF-677785. This research used resources of the Advanced Photon Source, a U.S. Department of Energy (DOE) Office of Science user facility at Argonne National Laboratory and is based on research supported by the U.S. DOE Office of Science-Basic Energy Sciences, under Contract No. DE-AC02-06CH11357.

Appendix A. Segmentation performance

To ascertain the reliability of our segmented data, we compare a digitally segmented image to one that is hand-segmented, taken as ground truth. All pixels are divided into four classes: true positives (TP), true negatives (TN), false positives (FP), and false negatives (FN). Mapping the pixels in this manner allows us to computed the average $recall\ (R)$, $precision\ (P)$, and F1-score for each of the three phases [66,67]. Sometimes called sensibility, recall describes the capability of a segmentation to identify all instances of a designated class $(i.e.,\ R=TP/(TP+FN))$. Meanwhile, precision, or sensitivity, describes the ability to identify only the designated class $(i.e.,\ P=TP/(TP+FP))$. Finally, the F1-score, otherwise known as the Dice loss score, gives the harmonic mean of the precision and recall $(i.e.,\ F_1=2(P*R)/(P+R)=2TP/(2TP+FN+FP))$. The recall, precision, and F1-score range from zero to one, with values closer to one indicating a higher accuracy.

To perform these calculations, we selected the central-most reconstructed slice for each of our time-steps and segmented it by hand, *i.e.*, tracing over the solid-solid interfaces as best as possible. We then compared each ground truth slice to the respective one automatically segmented and computed the precision, recall, and F1-score. In order to account for human error in the hand segmentation, we selected a tolerance threshold of 4 pixels (*i.e.*, 2% of image width and height). Table 3 gives the results. We find that the average recalls for Al, Al₂Cu, and Ag₂Al are 0.92 \pm 0.02, 0.92 \pm 0.01, and 0.99 \pm 0.01, respectively. Average precisions for Al, Al₂Cu, and Ag₂Al are 0.90 \pm 0.03, 0.92 \pm 0.02, and 0.97 \pm 0.1, respectively. Finally, the average F1-scores for Al, Al₂Cu, and Ag₂Al are 0.91 \pm 0.02, 0.92 \pm 0.01, and 0.98 \pm 0.01, respectively. All of these values display a high level of similarity and accuracy (comparable to other works [95,96]), confirming that our automated segmentation is reliable.

Appendix B. Supplementary data

Supplementary material related to this article can be found online at https://doi.org/10.1016/j.actamat.2024.119684.

Table 3 Contour matching scores. Recall, precision, and F1-score of the Al, Al_2Cu , and Ag_2Al phases computed by comparing automated and hand segmented images.

Time (hr.)	Recall			Precision		F1-score			
	Al	Al ₂ Cu	Ag ₂ Al	Al	Al ₂ Cu	Ag ₂ Al	Al	Al ₂ Cu	Ag ₂ Al
0	0.8846	0.9113	0.9885	0.8528	0.9256	0.9841	0.8684	0.9184	0.9863
0.5	0.9164	0.9226	0.9872	0.9355	0.9485	0.9819	0.9258	0.9354	0.9846
0.75	0.9311	0.9196	0.9989	0.9181	0.9419	0.9750	0.9246	0.9306	0.9868
1	0.9266	0.9209	0.9994	0.9067	0.9333	0.9803	0.9165	0.9271	0.9898
2	0.9226	0.9256	0.9932	0.8789	0.9004	0.9461	0.9002	0.9128	0.9691
3	0.9282	0.9300	0.9842	0.9022	0.8927	0.9628	0.9150	0.9110	0.9734
4	0.9330	0.9303	0.9987	0.9032	0.8886	0.9620	0.9178	0.9090	0.9800
Avg.	0.9203	0.9229	0.9929	0.8996	0.9187	0.9703	0.9098	0.9206	0.9814
Std.	0.067	0.0066	0.00631	0.0268	0.0245	0.0139	0.0201	0.0104	0.0076

References

- [1] J. Tang, R. Daiyan, M.B. Ghasemian, S.A. Idrus-Saidi, A. Zavabeti, T. Daeneke, J. Yang, P. Koshy, S. Cheong, R.D. Tilley, R.B. Kaner, R. Amal, K. Kalantar-Zadeh, Advantages of eutectic alloys for creating catalysts in the realm of nanotechnology-enabled metallurgy, Nature Commun. 10 (1) (2019) 1–14.
- [2] Chandra Sekhar Tiwary, Prafull Pandey, Suman Sarkar, Rakesh Das, Sumanta Samal, Krishanu Biswas, Kamanio Chattopadhyay, Five decades of research on the development of eutectic as engineering materials, Prog. Mater. Sci. 123 (February 2021) (2022) 100793.
- [3] S.K. Aramanda, K. Chattopadhyay, A. Choudhury, Exotic three-phase microstructures in the ternary Ag-Cu-Sb eutectic system, Acta Mater. 221 (2021) 117400.
- [4] U. Hecht, L. Granasy, T. Pusztai, B. Bottger, M. Apel, V. Witusiewicz, L. Ratke, J. De Wilde, L. Froyen, D. Camel, B. Drevet, G. Faivre, S.G. Fries, B. Legendre, S. Rex, Multiphase solidification in multicomponent alloys, Mater. Sci. Eng. R 46 (2004) 1-49.
- [5] Y. Wang, P. Chao, S. Moniri, J. Gao, T. Volkenandt, V. De Andrade, A.J. Shahani, Integrated three-dimensional characterization of reactive phase formation and coarsening during isothermal annealing of metastable Zn–3Mg–4Al eutectic, Mater. Charact. 170 (June) (2020) 110685.
- [6] P. Chao, G.R. Lindemann, A.H. Hunter, A.J. Shahani, Pseudo-4D view of the growth and form of locked eutectic colonies, Acta Mater. 240 (734) (2022) 1–46.
- [7] S.L. Allen, M.R. Notis, R.R. Chromik, R.P. Vinci, Microstructural evolution in lead-free solder alloys: Part I. Cast Sn-Ag-Cu eutectic, J. Mater. Res. 19 (5) (2004) 1417–1424.
- [8] S.L. Allen, M.R. Notis, R.R. Chromik, R.P. Vinci, D.J. Lewis, R. Schaefer, Microstructural evolution in lead-free solder alloy: Part II. Directionally solidified Sn-Ag-Cu, Sn-Cu and Sn-Ag, J. Mater. Res. 19 (5) (2004) 1425–1431.
- [9] J. van Suchtelen, Coarsening of eutectic structure during and after unidiretional growth, J. Cryst. Growth 43 (1978) 28–46.
- [10] J. Xie, S. Lu, Y. Du, W. Hu, Y. Mao, Microstructural evolution and orientation-correlated origin of the coarsening behaviors in Au–Sn eutectic alloys, J. Alloys Compd. 806 (2019) 1285–1291.
- [11] B. Cantor, G.A. Chadwick, Thermal stability of eutectic and off-eutectic Ag-Cu, Cd-Zn and Al-\(\xi\)(AlAg) alloys, J. Cryst. Growth 36 (2) (1976) 232–238.
- [12] S.A. Belyakov, R.J. Coyle, B. Arfaei, J.W. Xian, C.M. Gourlay, Microstructure and damage evolution during thermal cycling of Sn-Ag-Cu solders containing antimony, J. Electron. Mater. 50 (3) (2021) 825–841.
- [13] L. Fu, J. He, S. Lu, Y. Sun, D. Zhu, Y. Mao, Coarsening kinetics of lamellar and equiaxed microstructures of eutectic Au–20Sn during the annealing, J. Mater. Res. Technol. 17 (2022) 2134–2144.
- [14] A. Xue, X. Lin, L. Wang, X. Lu, H. Ding, W. Huang, Heat-affected coarsening of β grain in titanium alloy during laser directed energy deposition, Scr. Mater. 205 (2021) 114180.
- [15] M. Rafieazad, M. Ghaffari, A. Vahedi Nemani, A. Nasiri, Microstructural evolution and mechanical properties of a low-carbon low-alloy steel produced by wire arc additive manufacturing, Int. J. Adv. Manuf. Technol. 105 (5–6) (2019) 2121–2134.
- [16] H. Liu, H. Su, Z. Shen, D. Zhao, Y. Liu, Y. Guo, H. Guo, M. Guo, K. Xie, J. Zhang, L. Liu, H. Fu, One-step additive manufacturing and microstructure evolution of melt-grown Al₂O₃/GdAlO₃/ZrO₂ eutectic ceramics by laser directed energy deposition, J. Eur. Ceram. Soc. 41 (6) (2021) 3547–3558.
- [17] U. Hecht, A. Vayyala, P. Barriobero-Vila, N. Navaeilavasani, S. Gein, I. Cazic, J. Mayer, Microstructure evolution in the hypo-eutectic alloy Al_{0.75}CrFeNi_{2.1} manufactured by laser powder bed fusion and subsequent annealing, Mater. Sci. Eng. A 862 (November 2022) (2023) 144315.
- [18] R. Elliot, Eutectic Solidification Processing Crystalline and Glassy Alloys, Butterworths and Co., 1983, p. 375.
- [19] A.J. Ardell, Microstructural stability at elevated temperatures, J. Eur. Ceram. Soc. 19 (13–14) (1999) 2217–2231.
- [20] W. Kurz, D.J. Fisher, Fundamentals of Solidification, in: Retrospective Collection, Trans. Tech. Publications Limited, 1998.
- [21] J.A. Dantzig, M. Rappaz, Solidification, second ed., EPFL Press, 2016, p. 740.

- [22] M.A. Ruggiero, J.W. Rutter, Origin of microstructure in 350 K eutectic of Bi-In-Sn ternary system, Mater. Sci. Technol. (United Kingdom) 11 (2) (1995) 136–142.
- [23] S. Sengupta, H. Soda, A. McLean, Microstructure and properties of a bismuth-indium-tin eutectic alloy, J. Mater. Sci. 37 (9) (2002) 1747–1758.
- [24] Y. Wang, J. Gao, W. Sun, A.J. Shahani, In situ observation of faceted growth and morphological instability of a complex-regular eutectic in Zn–Mg–Al system, Scr. Mater. 206 (2022) 114224.
- [25] G.R. Lindemann, A.J. Shahani, Accelerated discovery of the Al-Ag₂Al-Al₂Cu eutectic coupled zone through genetic optimization, J. Alloys Compd. 827 (2020) 154.
- [26] G.R. Lindemann, P. Chao, A.H. Hunter, A.J. Shahani, Formation of three-phase eutectic grains on primary phases: Observations from correlative imaging, J. Alloys Compd. 923 (2022) 166274.
- [27] H.E. Cline, Shape instabilities of eutectic composites at elevated temperatures, Acta Metall. 19 (6) (1971) 481–490.
- [28] R.D. Doherty, Role of interfaces in kinetics of internal shape changes, Metal Sci. 16 (1) (1982) 1–14.
- [29] M.A. Matin, W.P. Vellinga, M.G.D. Geers, Aspects of coarsening in eutectic Sn-Pb, Acta Mater. 52 (12) (2004) 3475–3482.
- [30] R.H. Hopkins, R.W. Kraft, Nucleation and growth of the Pb-Sn eutectic, Trans. Metall. Soc. AIME 242 (1968) 1627–1633.
- [31] W.C. Holmes, Coarsening in Multiphase Multicomponent Systems Dissertation, 1999, p. 113.
- [32] W.C. Holmes, J.J. Hoyt, Particle coarsening in multiphase ternary systems, in: Materials Research Society Symposium - Proceedings, Vol. 580, 2000, pp. 248-253
- [33] C.J. Kuehmann, P.W. Voorhees, Ostwald ripening in ternary alloys, Metall. Mater. Trans. A 27 (4) (1996) 937–943.
- [34] G.C. Mukira, T.H. Courtney, Microconstituent development and coarsening in certain three-phase systems, Acta Mater. 44 (8) (1996) 3321–3329.
- [35] P. Steinmetz, S. Gadkari, A. Genau, Post-solidification effects in directionally solidified ternary eutectic Al-Ag₂Al-Al₂Cu, J. Cryst. Growth 507 (September 2018) (2019) 425–436.
- [36] N. D'Souza, L.M. Feitosa, G.D. West, H.B. Dong, Halo formation during solidification of refractory metal aluminide ternary systems, Metall. Mater. Trans. A 49 (5) (2018) 1749–1761.
- [37] P. Shi, R. Li, Y. Li, Y. Wen, Y. Zhong, W. Ren, Z. Shen, T. Zheng, J. Peng, X. Liang, P. Hu, N. Min, Y. Zhang, Y. Ren, P.K. Liaw, D. Raabe, Y.D. Wang, Hierarchical crack buffering triples ductility in eutectic herringbone high-entropy alloys, Science 373 (6557) (2021) 912–918.
- [38] R.H. Mathiesen, L. Arnberg, F. Mo, T. Weitkamp, A. Snigirev, Time resolved X-ray imaging of dendritic growth in binary alloys, Phys. Rev. Lett. 83 (24) (1999) 5062–5065.
- [39] R.H. Mathiesen, L. Arnberg, K. Ramsøskar, T. Weitkamp, C. Rau, A. Snigirev, Time-resolved X-ray imaging of aluminum alloy solidification processes, Metall. Mater. Trans. B 33 (4) (2002) 613–623.
- [40] R.H. Mathiesen, L. Arnberg, X-ray radiography observations of columnar dendritic growth and constitutional undercooling in an Al 30wt % Cu alloy, Acta Mater. 53 (2005) 947–956.
- [41] R.H. Mathiesen, L. Arnberg, H. Nguyen-Thi, B. Billia, In situ X-ray video microscopy as a tool in solidification science, Jom 64 (1) (2012) 76–82.
- [42] D.G. Mccartney, J.D. Hunt, R.M. Jordan, The structures expected in a simple ternary eutectic system: Part II. The Al-Ag-Cu Ternary System, Metall. Trans. A 11 (8) (1980) 1243–1249.
- [43] A. Dennstedt, L. Ratke, Microstructures of directionally solidified Al-Ag-Cu ternary eutectics, Trans. Indian Inst. Met. 65 (6) (2012) 777–782.
- [44] A. Genau, L. Ratke, Morphological characterization of the Al-Ag-Cu ternary eutectic, Int. J. Mater. Res. 103 (4) (2012) 469–475.
- [45] J. De Wilde, E. Nagels, F. Lemoisson, L. Froyen, Unconstrained growth along a ternary eutectic solidification path in Al-Cu-Ag: Preparation of a MAXUS sounding rocket experiment, Mater. Sci. Eng. A 413–414 (2005) 514–520.

- [46] P. Steinmetz, J. Hötzer, A. Dennstedt, C. Serr, B. Nestler, A. Genau, Graph-based investigation of three-dimensional microstructure rearrangement during ternary eutectic directional solidification of Al-Ag-Cu, J. Cryst. Growth 498 (June) (2018) 230–243
- [47] U. Hecht, I. Sargin, P. Steinmetz, A. Genau, M. Şerefo' glu, A. Dennstedt, Crystal orientation relationships in ternary eutectic Al-Al₂Cu-Ag₂Al, Acta Mater. 157 (2018) 96–105.
- [48] I. Sargin, Invariant and Univariant Eutectic Solidification in Ternary Alloys (Ph.D. thesis), Iowa State University, 2015, pp. 1–173.
- [49] J. Friess, P. Rayling, U. Hecht, A. Genau, Impact of crystal orientation relationship on microstructure evolution in Al-Ag-Cu ternary eutectic, J. Cryst. Growth (2022) 126799.
- [50] I. Sargin, A.L. Genau, R.E. Napolitano, Post-solidification effects in directionally grown Al-Ag₂Al-Al₂Cu eutectics, J. Phase Equilibria Diffusion 37 (1) (2016) 75–85.
- [51] A. Dennstedt, A. Choudhury, L. Ratke, B. Nestler, Microstructures in a ternary eutectic alloy: Devising metrics based on neighbourhood relationships, IOP Conf. Ser.: Mater. Sci. Eng. 117 (1) (2016).
- [52] A. Dennstedt, L. Helfen, P. Steinmetz, B. Nestler, L. Ratke, 3D synchrotron imaging of a directionally solidified ternary eutectic, Metall. Mater. Trans. A 47 (3) (2016) 981–984.
- [53] X. Li, J. Wang, L. Hou, A. Gagnoud, Y. Fautrelle, Studying on the morphology of primary phase by 3D-CT technology and controlling eutectic growth by tailoring the primary phase, J. Alloys Compd. 821 (2020).
- [54] A.J. Shahani, X. Xiao, E.M. Lauridsen, P.W. Voorhees, Characterization of metals in four dimensions. Mater. Res. Lett. 8 (12) (2020) 462–476.
- [55] R. Trivedi, H. Miyahara, P. Mazumder, E. Simsek, S.N. Tewari, Directional solidification microstructures in diffusive and convective regimes, J. Cryst. Growth 222 (1–2) (2001) 365–379.
- [56] V. De Andrade, A. Deriy, M.J. Wojcik, D. Gürsoy, D. Shu, K. Fezzaa, F. De Carlo, Nanoscale 3D imaging at the advanced photon source, 2016, SPIE Newsroom.
- [57] V. De Andrade, V. Nikitin, M. Wojcik, A. Deriy, S. Bean, D. Shu, T. Mooney, K. Peterson, P. Kc, K. Li, S. Ali, K. Fezzaa, D. Gürsoy, C. Arico, S. Ouendi, D. Troadec, P. Simon, F. De Carlo, C. Lethien, Fast X-ray nanotomography with sub-10 nm resolution as a powerful imaging tool for nanotechnology and energy storage applications, Adv. Mater. 33 (21) (2021) 1–11.
- [58] V. Nikitin, V. De Andrade, A. Slyamov, B.J. Gould, Y. Zhang, V. Sampathkumar, N. Kasthuri, D. Gürsoy, F. De Carlo, Distributed optimization for nonrigid nano-tomography, IEEE Trans. Comput. Imaging 7 (2021) 272–287.
- [59] D. Gürsoy, F. De Carlo, X. Xiao, C. Jacobsen, TomoPy: A framework for the analysis of synchrotron tomographic data, J. Synchrotron Radiat. 21 (5) (2014) 1188–1193.
- [60] A.C. Kak, M. Slaney, Principles of Computerized Tomographic Imaging, SIAM, 2001
- $\hbox{\bf [61]} \ \ F. \ Natterer, \ The \ Mathematics \ of \ Computerized \ Tomography, \ SIAM, \ 2001.$
- [62] S. Boyd, N. Parikh, E. Chu, B. Peleato, J. Eckstein, Distributed optimization and statistical learning via the alternating direction method of multipliers, Found. Trends[®] Mach. Learn. 3 (1) (2011) 1–122.
- [63] J. De Wilde, L. Froyen, S. Rex, Coupled two-phase $[a(Al) + \theta(Al_2Cu)]$ planar growth and destabilisation along the univariant eutectic reaction in Al-Cu-Ag alloys. Scr. Mater. 51 (6) (2004) 533–538.
- [64] J. Hötzer, P. Steinmetz, A. Dennstedt, A. Genau, M. Kellner, I. Sargin, B. Nestler, Influence of growth velocity variations on the pattern formation during the directional solidification of ternary eutectic Al-Ag-Cu, Acta Mater. 136 (2017) 335–346
- [65] R. Manser, R. Elsässer, V. Döring, ZEISS ZEN intellesis machine learning approaches for easy and precise image segmentation, 2018, Zeiss.
- [66] Alex P. Zijdenbos, Benoit M. Dawant, Richard A. Margolin, Andrew C. Palmer, Morphometric Analysis of White Matter Lesions in MR Images: Method and Validation, IEEE Trans. Med. Imaging 13 (4) (1994) 716–724.
- [67] Davide Chicco, Giuseppe Jurman, The advantages of the Matthews correlation coefficient (MCC) over F1 score and accuracy in binary classification evaluation, BMC Genomics 21 (1) (2020) 1–13.
- [68] M. Botsch, L. Kobbelt, M. Pauly, P. Alliez, B. Lévy, Polygon mesh processing, CRC Press, 2010.
- [69] M. De Graef, A dictionary indexing approach for EBSD, IOP Conference Series: Materials Science and Engineering 891 (1) (2020).

[70] F. Bachmann, R. Hielscher, H. Schaeben, Texture Analysis with MTEX – Free and Open Source Software Toolbox, in: Texture and Anisotropy of Polycrystals III, in: Solid State Phenomena, 160, Trans Tech Publications Ltd, 2010, pp. 63–68.

- [71] The MathWorks Inc., MATLAB version: 9.13.0 (R2022b), The MathWorks Inc., Natick, Massachusetts, United States, 2022.
- [72] D. Du, Y. Fautrelle, Z. Ren, R. Moreau, X. Li, Effect of a high magnetic field on the growth of ternary Al-Cu-Ag alloys during directional solidification, Acta Mater. 121 (2016) 240–256.
- [73] A.J. Shahani, E.B. Gulsoy, S.O. Poulsen, X. Xiao, P.W. Voorhees, Twin-mediated crystal growth: An enigma resolved, Sci. Rep. 6 (1) (2016) 28651.
- [74] P. Chao, G.R. Lindemann, A.H. Hunter, A.J. Shahani, Pseudo-4D view of the growth and form of locked eutectic colonies, Acta Mater. 240 (2022) 118335.
- [75] O. Engler, V. Randle, Introduction to Texture Analysis, second ed., CRC Press, 2009, pp. 1–488.
- [76] M. Niewczas, Lattice correspondence during twinning in hexagonal close-packed crystals, Acta Mater. 58 (17) (2010) 5848–5857.
- [77] A. Choudhury, Y.C. Yabansu, S.R. Kalidindi, A. Dennstedt, Quantification and classification of microstructures in ternary eutectic alloys using 2-point spatial correlations and principal component analyses, Acta Mater. 110 (2016) 131–141.
- [78] V.T. Witusiewicz, U. Hecht, S.G. Fries, S. Rex, The Ag-Al-Cu system II. A thermodynamic evaluation of the ternary system, J. Alloys Compd. 385 (1-2) (2004) 133-143.
- [79] N.L. Peterson, S.J. Rothman, Impurity diffusion in aluminum, Phys. Rev. B 1 (8) (1970) 3264–3273.
- [80] J. Kang, N. Lu, I. Loo, N. Senabulya, A.J. Shahani, PolyProc: A modular processing pipeline for X-ray diffraction tomography, Integr. Mater. Manuf. Innov. 8 (3) (2019) 388–399.
- [81] A.J. Ardell, Isotropic fiber coarsening in unidirectionally solidified eutectic alloys, Metall. Trans. 3 (1972) 1395–1401.
- [82] M. Ferrante, R.D. Doherty, Influence of interfacial properties on the kinetics of precipitation and precipitate coarsening in aluminium-silver alloys, Acta Metall. 27 (10) (1979) 1603–1614.
- [83] A.J. Ardell, Experimental confirmation of the Lifshitz Wagner theory of particle coarsening, in: The Mechanism of Phase Transformations in Crystalline Solids, Inst. of Metals, 1969, pp. 111–116.
- [84] I.M. Lifshitz, V.V. Slyozov, The kinetics of precipitation from supersaturated solid solutions, J. Phys. Chem. Solids 19 (1–2) (1961) 35–50.
- [85] C. Wagner, Theorie der Alterung, Zeitschrift für Elektrochemie, Berichte der Bunsengesellschaft für physikalische Chemie 65 (7–8) (1961) 581–591.
- [86] P.W. Voorhees, Ostwald ripening of two-phase mixtures, Annu. Rev. Mater. Sci. 22 (1) (1992) 197–215.
- [87] D. Fan, S.P. Chen, L. Chen, P.W. Voorhees, Phase-field simulation of 2-D Ostwald ripening in the high volume fraction regime, Acta Mater. 50 (8) (2002) 1895–1907.
- [88] L.D. Graham, R.W. Kraft, Coarsening of eutectic microstructures at elevated temperatures, Trans. Metall. Soc. AIME 236 (1) (1966) 94–102.
- [89] G.C. Weatherly, An electron-microscope investigation of the lamellar Al-CuAl₂ eutectic, Metal Sci. J. 2 (1) (1968) 25–27.
- [90] S.P. Marsh, M.E. Glicksman, Overview of geometric effects on coarsening of mushy zones, Metall. Mater. Trans. A 27 (1996) 557–567.
- [91] R.W. Kraft, Crystallography of equilibrium phase interfaces, Trans. Metall. Soc. AIME 224 (February) (1962) 65–75.
- [92] Z. Zhang, J.M. Rosalie, N.V. Medhekar, L. Bourgeois, Resolving the FCC/HCP interfaces of the γ' (Ag₂Al) precipitate phase in aluminium, Acta Mater. 174 (2019) 116–130.
- [93] V. Kokotin, U. Hecht, Molecular dynamics simulations of $Al-Al_2Cu$ phase boundaries, Comput. Mater. Sci. 86 (2014) 30–37.
- [94] OpenAI, ChatGPT version: July 2023, 2023, https://openai.com/research/ chatgpt.
- [95] Yunwei Gui, Kenta Aoyagi, Huakang Bian, Akihiko Chiba, Detection, classification and prediction of internal defects from surface morphology data of metal parts fabricated by powder bed fusion type additive manufacturing using an electron beam, Addit. Manuf. 54 (March) (2022) 102736.
- [96] Jiwon Yeom, Tiberiu Stan, Seungbum Hong, Peter W. Voorhees, Segmentation of experimental datasets via convolutional neural networks trained on phase field simulations, Acta Mater. 214 (2021) 116990.